Main Manuscript for

Structural Insights into Biased Signaling at Chemokine Receptor CCR7

Kotaro Tanaka[1], Kouki Nishikawa[2], Yuki Shiimura[3,4],
Yoshinori Fujiyoshi[1], and Naotaka Tsutsumi[1*]

[1] Advanced Research Initiative, Institute of Integrated Research, Institute of Science Tokyo, Bunkyo, Tokyo 113-8510, Japan.
[2] Joint Research Course for Advanced Biomolecular Characterization, Faculty of Agriculture, Tokyo University of Agriculture and Technology, Fuchu, Tokyo 183-8509, Japan.
[3] Division of Molecular Genetics, Institute of Life Science, Kurume University, Fukuoka 830-0011, Japan.
[4] Department of Cell Biology, Graduate School of Medicine, Kyoto University, Kyoto 606-8501, Japan.

***Corresponding author**: Naotaka Tsutsumi
Email: tsutsumi.naotaka@tmd.ac.jp

Author contributions:
KT: Data Curation (equal), Formal Analysis (lead), Investigation (supporting), Methodology (equal), Software (lead), Validation (equal), Visualization (equal), Writing – Original Draft (supporting), Writing – Review & Editing (equal). KN: Data Curation (supporting), Investigation (equal), Writing – Review & Editing (supporting). YS: Data Curation (supporting), Investigation (equal), Methodology (equal), Writing – Review & Editing (equal). YF: Funding acquisition (lead),

Methodology (equal), Resource (lead), Supervision (equal), Writing – Review & Editing (supporting). NT: Conceptualization (lead), Data Curation (equal), Formal Analysis (supporting), Funding Acquisition (supporting), Investigation (lead), Methodology (equal), Project Administration (lead), Resources (supporting), Software (supporting), Supervision (equal), Validation (equal), Visualization (equal), Writing – Original Draft (lead), Writing – Review & Editing (lead).

Competing interests:

The authors declare no competing interests.

Classification:

Biological Sciences

Biophysics and Computational Biology

Keywords:

CCR7, Chemokine, Cryo-EM, MD Simulations, Signaling Bias

This PDF file includes:

Main Text

Figures 1 to 6

Abstract：

CC chemokine receptor 7 (CCR7), which orchestrates adaptive immunity, exhibits a phenomenon known as biased agonism. CCL19 induces robust G protein signaling and β-arrestin recruitment, leading to transient signaling. In contrast, CCL21 preferentially activates G protein pathways with minimal arrestin engagement, resulting in sustained signaling and differential functional outcomes. Here, we present the cryo-EM structures of the human CCR7-G_i complex with either CCL19 or CCL21. The structures reveal that while both engage a conserved orthosteric pocket, they adopt markedly distinct binding poses. Notably, the compact 30s loop of CCL21 inserts deeply into the receptor's extracellular vestibule, whereas the corresponding loop of CCL19 rests atop extracellular loop 2. Molecular dynamics simulations further reveal that these distinct binding modes induce differential intracellular dynamics, linked to the rotameric state of Y83 at the intracellular end of transmembrane helix 1. We demonstrate that CCL19 stabilizes a flexible conformational ensemble with a highly dynamic helix 8, creating a lateral opening favorable for GPCR kinase engagement. Conversely, CCL21 restricts this flexibility, locking the receptor in a state that precludes kinase interaction while maintaining G protein coupling. Corroborated by functional data, these findings provide key insights into the structural basis of biased agonism at CCR7 and establish a foundation for rational design of pathway-selective immunomodulators.

Significance statement:

Chemokine receptor CCR7 directs immune cell migration by activating distinct signaling pathways in response to CCL19 and CCL21, a phenomenon known as biased agonism. The structural basis for this divergence has remained unclear. By combining cryo-electron microscopy with molecular dynamics simulations, we reveal that although both ligands stabilize similar G protein-bound conformations, they drive distinct receptor dynamics. We demonstrate that CCL19 induces a flexible intracellular conformation necessary for recruiting regulatory kinases, whereas CCL21 locks the receptor in a state precluding this interaction. This "dynamic selection" model aligns with functional data and rationalizes a fundamental paradox in

77 chemokine biology, highlighting the critical role of protein dynamics in signal transduction and
78 providing a blueprint for designing precision immunotherapeutics.

Main Text

Introduction

Adaptive immunity relies on the precise spatiotemporal orchestration of immune cell positioning and activation to mount effective responses against pathogens and malignant cells while maintaining self-tolerance (1, 2). Central to this process is CC chemokine receptor 7 (CCR7) (SI Appendix, Fig. S1A), a G protein-coupled receptor (GPCR) that governs the trafficking of various T cells, mature dendritic cells (DCs), and B cells to secondary lymphoid organs (SLOs) (3–7). Its two endogenous ligands, CC chemokine ligand 19 (CCL19) and 21 (CCL21), form chemotactic gradients within SLOs to guide CCR7-expressing cells (8–11). This homing mechanism is essential for bringing naïve T cells into close proximity with antigen-presenting DCs within the T cell zones of SLOs, a prerequisite for T cell priming and the initiation of antigen-specific immunity (12). Given its pivotal role, the CCR7 axis is a critical therapeutic target for a broad spectrum of human pathologies (13–15). Hyperactive CCR7 signaling promotes cancer metastasis and autoimmune disorders, whereas insufficient activity impairs immune surveillance and vaccine efficacy, highlighting the need for precisely tuned modulators.

However, effectively targeting this axis is complicated by the phenomenon of biased agonism, for which the CCR7 system is a paradigmatic example in the chemokine family (16). Although both ligands engage the same receptor, they induce strikingly different downstream signaling profiles and cellular responses (SI Appendix, Fig. S1B) (17–20). While sharing a structurally conserved core chemokine domain, CCL21 possesses a unique, highly basic C-terminal tail absent in CCL19 (SI Appendix, Fig. S1C). This tail facilitates binding to glycosaminoglycans (GAGs) on cell surfaces and in the extracellular matrix, which is crucial for establishing stable chemotactic gradients and facilitating haptotaxis (20–22). Beyond GAG interactions, their in vivo profiles are shaped by atypical chemokine receptors: CCRL2 selectively sequesters CCL19, whereas ACKR4 scavenges both (23–25). Nevertheless, the fundamental functional divergence is generally thought to be primarily driven by their biased agonism directly at CCR7.

Functionally, CCL19 potently induces G protein activation and β-arrestin recruitment. This process is mediated by receptor phosphorylation via GPCR kinases (GRKs), specifically

108 GRK3 and GRK6, leading to potent but transient G protein signaling characterized by rapid
109 receptor desensitization and internalization (17–19). In contrast, CCL21 activates G protein
110 signaling with a potency initially reported to be comparable to, or approximately 10-fold lower
111 than, that of CCL19, but it inefficiently recruits β-arrestin following phosphorylation solely by
112 GRK6, resulting in minimal internalization (17–20). This differential regulation is physiologically
113 crucial. The acute nature of CCL19 signaling facilitates localized cellular activation and precise
114 positioning within SLOs, whereas the sustained signaling induced by CCL21, combined with
115 GAG-regulated localization, establishes the stable, long-range chemotactic gradients required
116 for guiding cell migration over distances (22, 26–28).

117 Despite its profound physiological importance, the mechanism by which these two
118 distinct chemokines elicit biased signaling through CCR7 has been a long-standing enigma (29).
119 Understanding the molecular mechanisms underlying this bias requires elucidating how ligand
120 binding translates into distinct receptor conformations that selectively engage G proteins
121 versus GRKs and arrestins. While the crystal structure of inactive-state CCR7 bound to the
122 small-molecule intracellular antagonist Cmp2105 provided valuable insights into inhibitor
123 binding (15), the structural underpinnings of its activation by endogenous chemokines remain
124 elusive.

125 Here, we report the cryo-electron microscopy (cryo-EM) structures of human CCR7 in
126 complex with CCL19 and CCL21, each stabilized in an active conformation by the heterotrimeric
127 inhibitory G protein (G_i). These structures reveal distinct ligand binding modes and differential
128 receptor conformations induced by the two chemokines. The structures illustrate a unique
129 mechanism of receptor activation shared within the CCR7-like chemokine receptor subfamily.
130 Concurrently, while the overall G_i binding mode is similar, subtle conformational differences in
131 intracellular regions not directly involved in G_i binding, such as ICL1, suggest distinct
132 downstream signaling profiles. Motivated by these distinctions, we performed molecular
133 dynamics (MD) simulations to detail the dynamic basis for these structural differences after G
134 protein dissociation. These simulations revealed substantial differences in receptor
135 conformational equilibria, especially in helix 8 (H8), that might influence GRK recruitment.
136 Importantly, structure-guided mutagenesis targeting this intracellular network selectively

137 impaired arrestin recruitment, supporting these computational findings and validating our
138 hypothesis regarding the dynamic control of transducer selectivity. This study elucidates the
139 structural basis for G protein activation by two distinct chemokines, providing fundamental
140 insights into the mechanism of biased agonism at CCR7 and offering a structural template for
141 the rational design of pathway-selective agonists.
142
143 **Results**
144 **Preparation and overall architecture of the active CCR7-G_i complexes**
145 To elucidate the structural basis of CCR7 signaling, we utilized a robust strategy to
146 assemble stable, active-state complexes for cryo-EM (SI Appendix, Fig. S2 and Methods). We
147 employed a temporally controlled expression system in tetracycline-inducible Expi293F
148 (Expi293Fi) cells, expressing an engineered G_i heterotrimer prior to human CCR7 to maximize
149 receptor stability and complex formation efficiency (SI Appendix, Fig. S2A). The G_i complex
150 incorporated a single-chain Gγ-Gα_i fusion (30) with dominant negative Gα_i mutations (31) for
151 enhanced stability. Additionally, the receptor and G protein were non-covalently tethered using
152 the NanoBiT system (LgBiT fused to CCR7 and HiBiT fused to Gβ) (32, 33). The ligand-free CCR7-
153 G_i complex, further stabilized by the fiducial marker scFv16 (34), was purified and the final
154 signaling complexes were formed by adding separately purified full-length CCL19 or CCL21,
155 yielding viable samples for cryo-EM analysis (SI Appendix, Fig. S2B-F).
156 Single-particle cryo-EM analysis of the samples yielded high-resolution maps with
157 nominal resolutions of 3.0 Å for the CCL19-CCR7-G_i-scFv16 complex and 3.2 Å for the CCL21-
158 CCR7-G_i-scFv16 complex (Fig. 1A, and SI Appendix, Table S1 and Fig. S3-S6). During 3D
159 classification, we observed structural heterogeneity related to post-translational modifications
160 (glycosylation at N36 and N292 of CCR7) and weak densities suggesting partial ordering of the
161 proximal CCL21 C-terminal tail. However, as these classes represented minor populations and
162 exhibited lower local resolution at the core interface, we focused on the most homogeneous
163 particle subsets to accurately define the primary ligand binding modes.
164 The overall architecture of the complexes resembles previously reported GPCR-G
165 protein structures, characterized by the canonical insertion of the Gα_i-α5 helix into the

166 receptor's cytoplasmic core (Fig. 1A-C). The seven-transmembrane (7TM) conformations of
167 CCR7 in both structures are essentially identical, with a Cα root-mean-square deviation (RMSD)
168 of 0.36 Å. They also exhibit a highly similar docking mode for the G_i heterotrimer (Cα RMSD of
169 1.48 Å). Strikingly, however, the chemokines themselves adopt distinct orientations, reflected
170 in a substantial Cα RMSD of 4.31 Å when aligning the complexes based on the receptor (Fig. 1B).
171

172 **A lateral TM6 movement during CCR7 activation**

173 To understand the conformational changes associated with CCR7 activation, we
174 compared the CCL19-bound active-state structure with the inactive CCR7 structure bound to
175 the intracellular antagonist Cmp2105 (15) to elucidate the general mode of activation in
176 comparison with other chemokine receptor systems (Fig. 1C). Both CCL19 and CCL21 induce a
177 similar global conformational rearrangement in CCR7, creating a cytoplasmic cavity to
178 accommodate the G protein.

179 The most prominent feature of this transition is the outward movement of
180 transmembrane helix 6 (TM6). Unlike the canonical hinge-like pivot observed in most class A
181 GPCRs, including CCR2 and CXCR2 (35, 36), CCR7 exhibits a predominantly parallel outward shift
182 of TM6 by 3-4 Å (Fig. 1D). Specifically, the entire TM6 helix, from its extracellular end to its
183 intracellular tip, moves laterally as a semi-rigid unit away from the receptor's central axis. This
184 activation mode is similar to that observed in its paralog, CCR6 (34% sequence identity), which
185 also shows a ~5 Å global shift (37).

186 These distinct activation modes correlate with the presence or absence of the critical
187 $W^{6.48}$ residue within the CWxP motif (superscripts denote Ballesteros-Weinstein numbering)
188 (Fig. 1D). In most class A GPCRs, $W^{6.48}$ acts as a rotamer "toggle switch," initiating
189 conformational changes that displace the intracellular half of TM6 (36, 38). In CCR7 and CCR6,
190 this tryptophan is replaced by glutamine ($Q^{6.48}$). We propose that this subclass-specific
191 activation pathway is structurally encoded in the inactive state (Fig. 1E). In CCR7 and CCR6, the
192 less bulky $Q^{6.48}$ allows the extracellular portion of TM6 to pack closer to the receptor's central
193 axis, closely approaching the bulky $F^{3.36}$ on TM3. Furthermore, a hydrogen-bond network
194 centered on $Y^{3.32}$ stabilizes the extracellular ends of TM3 and TM6 in close proximity. Upon

195 activation, the insertion of the bulky chemokine core acts as a wedge, forcing the entire TM6
196 laterally outward while the extracellular end of TM5 concurrently closes inward to clasp the
197 ligand. In contrast, in canonical receptors like CCR2 and CXCR2, the bulky $W^{6.48}$ restricts TM6
198 from closely approaching $F/Y^{3.36}$ due to steric hindrance, enforcing a wider extracellular gap
199 between TM3 and TM6. Because the extracellular segment of TM6 is already pre-opened in the
200 inactive state, chemokine binding induces minimal outward movement at this site. Instead,
201 activation primarily triggers the microswitch-driven opening of the intracellular half, producing
202 the classic pivot movement.
203
204 **Distinct binding modes of CCL19 and CCL21 dictated by CRS3 interactions**
205 The most pronounced differences between the two active complexes are found at the
206 extracellular ligand-recognition interface. Strikingly, the core domain of CCL21 is globally
207 rotated by 17.6° relative to CCL19 when viewed from the side of the receptor (Fig. 2A). This
208 rotation results in significantly altered interaction interfaces, with a larger buried surface area
209 for CCL21 (1,640 $Å^2$) compared to CCL19 (1,380 $Å^2$).
210 Chemokine recognition generally follows an expanded "two-site" model (39), involving
211 interactions across several chemokine recognition sites (CRS): CRS1 (receptor N-
212 terminus/chemokine core), CRS1.5 (receptor N-loop and ECL3/chemokine N-loop), CRS2
213 (receptor 7TM pocket/chemokine N-terminus), and CRS3 (receptor ECL2/chemokine 30s loop)
214 (SI Appendix, Fig. S7A). Our structures reveal that the dramatic difference in orientation stems
215 primarily from divergent interactions at CRS3 (Fig. 2B).
216 Despite overall sequence conservation (32% identity, 68% similarity in the core region;
217 SI Appendix, Fig. S1C), the 30s loops of CCL19 and CCL21 exhibit distinct sequences and
218 conformations (Fig. 2B,C). The CCL21 loop (^{28}QEPS**L**GCSIP^{37}) is notably less bulky and more
219 hydrophobic at the center than the corresponding loop in CCL19 (^{28}LLIK**D**GCRVP^{37}), featuring
220 L32 instead of D32 (Fig. 2C). Consequently, the 30s loop of CCL19 adopts a curled conformation
221 and rests atop CCR7-ECL2. In contrast, the more compact 30s loop of CCL21 penetrates deeper
222 into the extracellular pocket. Crucially, CCL21-L32 inserts like a wedge between the chemokine

223 N-terminus and CCR7-L212^{ECL2} (Fig. 2B,D). This deep insertion stabilizes a specific conformation
224 of ECL2 and contributes to the overall rotation of CCL21.

225 In contrast to the divergent CRS3 interactions, the engagements at CRS1 and CRS2 are
226 relatively conserved. At CRS1, CCR7-F44 forms the core of the interactions with the chemokine
227 bodies (SI Appendix, Fig. S7B). At CRS2, the N-terminal loops of both chemokines penetrate the
228 "minor orthosteric binding pocket" of CCR7 surrounded by TM1, TM2, TM3, TM6, and TM7,
229 forming extensive polar and hydrophobic interactions (Fig. 2D) (40). The N-terminus of CCL19
230 penetrates slightly deeper into the pocket than that of CCL21. Specifically, the sidechain of
231 CCL19-T2 engages Y136$^{3.32}$ at TM3, inducing a subtle shift of this residue. The observed CRS2
232 interaction networks generally correlate with reported receptor mutagenesis data (41). For
233 example, CCR7 residues K50$^{N\text{-term}}$ and R54$^{N\text{-term}}$ are located at the tip of TM1 and the center of
234 the molecular interface, forming critical contacts with the N-terminal peptides of both
235 chemokines (Fig. 2D). This explains why the CCR7-K50A$^{N\text{-term}}$ and CCR7-R54A$^{N\text{-term}}$ mutations
236 dramatically impair both CCL19- and CCL21-induced signaling. Conversely, the CCR7-R209A^{ECL2}
237 mutation selectively reduces CCL19-induced signaling. This selectivity is structurally rationalized
238 by the more extensive polar contacts of R209^{ECL2} with the N-terminus/core of CCL19, via the
239 D4/E6 sidechains and D32 backbone, compared to CCL21 (Fig. 2D), highlighting its specific role
240 in CCL19 recognition.

241 These distinct binding modes result in ligand-specific conformational shifts in the
242 extracellular portions of TM1, TM3, TM5, TM7, and ECL2 (Fig. 2E and SI Appendix, Fig. S7C).
243 Furthermore, these differences propagate to an aromatic cluster located in the middle layer of
244 the minor pocket, just beneath the chemokine N-termini (Fig. 2F and SI Appendix, Fig. S7B).
245 Residues Y65$^{1.39}$, Y136$^{3.32}$, Y279$^{6.51}$, and Y312$^{7.39}$ exhibit distinct conformations in the inactive,
246 CCL21-bound, and CCL19-bound states, with the CCL19-bound state exhibiting consistently
247 more extensive changes. Among these residues, the Y312$^{7.39}$E mutation is known to confer a
248 high degree of constitutive activity to CCR7 while abolishing chemokine sensitivities, whereas
249 Y312$^{7.39}$A only causes high basal activities, underscoring the importance of this residue for the
250 inactive-to-active transition (20). The correlated rearrangements in the aromatic network likely

251 contribute to the differential stabilization of active-state conformations and may underlie the
252 observed differences in general signaling potency (CCL19 > CCL21) (20).
253
254 **Structural basis of CCR7 activation and core G protein interface**
255 The binding of both chemokines induces canonical conformational changes associated
256 with class A GPCR activation (38) (Fig. 3A), although with the unique features related to TM6
257 movement described earlier. The PIF-like motif ($P^{5.50}$-$M^{3.40}$-$F^{6.44}$) undergoes reorganization,
258 characterized by the movement of the $M144^{3.40}$ sidechain, which induces inward and outward
259 shifts of TM5 and TM6, respectively (Fig. 3A, bottom left). The immediately downstream
260 hydrophobic lock collapses to further destabilize the inactive state (Fig. 3A, bottom center).
261 Concurrently, the sodium-binding site, which is stabilized by sodium ion coordination
262 with $N76^{1.50}$, $D104^{2.50}$, $N322^{7.49}$, and $Y326^{7.53}$ in the inactive state, collapses upon activation,
263 accompanied by the kinking of the $NP^{7.50}$xxY motif at TM7 and the flipping of the $Y326^{7.53}$
264 sidechain (Fig. 3A, top right). At the same time, the $DR^{3.50}$Y motif reorganizes, allowing $R154^{3.50}$
265 to form a bridge with $Y326^{7.53}$, thereby stabilizing the active conformation for G protein
266 coupling (Fig. 3A, bottom right).
267 Comparing these active states with the Cmp2105-bound inactive structure highlights the
268 structural rearrangements required for G protein engagement (Fig. 3B, top left). The outward
269 movement of TM6 and the concomitant shift of TM5 create the binding pocket for the $G\alpha_i$
270 subunit, prompting significant reorganization of the intracellular loops. Notably, ICL2 transitions
271 from a disordered loop in the inactive state to a stable, short α-helix upon activation, which is
272 critical for engaging the Gα subunit. Similarly, ICL3 is stabilized following TM6 displacement to
273 further form the G protein interface. Cmp2105 stabilizes the inactive state by preventing this
274 conformational shift and sterically occluding the binding site of the $G\alpha_i$-α5 helix (Fig. 3B, top
275 right).
276 The primary interface between CCR7 and $G\alpha_i$ involves the insertion of the C-terminal α5-
277 helix of $G\alpha_i$ deep into the cytoplasmic cavity of the receptor (Fig. 1A-C and 3B). This highly
278 conserved interface is stabilized by extensive interactions in both the CCL19- and CCL21-bound
279 complexes (Fig. 3B, bottom panels). The $G\alpha_i$-F(-1) [F354] sidechain is sandwiched between

280 E257$^{6.29}$ and K260$^{6.32}$, positioning its C-terminal carboxyl group for polar interactions with the
281 backbone amide at the TM7-H8 turn and the K260$^{6.32}$ sidechain. The L(-2) [L353] sidechain
282 inserts into a hydrophobic pocket formed by TM6 residues and R154$^{3.50}$ at TM3, capped by L(-7)
283 [L348]. Additionally, the R154$^{3.50}$ sidechain forms polar interactions with the C(-4) [C351]
284 backbone carbonyl. Despite minor variations at the periphery of the core interface, the overall
285 interaction patterns remain highly conserved.
286
287 **Subtle differences at the intracellular loops suggest distinct signaling outcomes**
288 Despite the overall similarity in G protein coupling, a detailed comparison reveals subtle
289 but notable differences in the intracellular loops between the CCL19- and CCL21-bound
290 complexes (Fig. 4A,B).
291 The conformations of ICL2 and ICL3, which form the major part of the G_i interface, are
292 essentially identical in both active structures. In the ICL2 region, the interactions between CCR7
293 residues (e.g., H165, R166) and the $G\alpha_i$ αN-β1 hinge region (e.g., R32, D193) are conserved,
294 exhibiting minor variations (Fig. 4A,B, top left panels). Similarly, the core interface mediated by
295 ICL3, TM5, and TM6 is highly conserved (Fig. 4A,B, bottom left panels).
296 In contrast, ICL1, which is less directly involved in the primary G_i interface, adopts
297 distinct loop conformations in the two complexes (Fig. 4A,B, bottom right panels). This
298 divergence appears to originate from differences in the side-chain conformation of Y83$^{1.57}$,
299 located at the cytoplasmic end of TM1. The distinct binding modes of CCL19 and CCL21 induce
300 specific rearrangements in the extracellular TMs (Fig. 2D) and the central aromatic network (Fig.
301 2F). This network appears to function as an allosteric link, propagating these differences
302 through the helical bundle (particularly TM1) to induce the distinct rotameric states of Y83$^{1.57}$ in
303 the CCL19- versus CCL21-bound structures. These states influence the length of TM1 and the
304 positioning of adjacent residues, propagating to the overall conformation of the ICL1 loop.
305 To investigate the functional relevance of the observed structural differences, we first
306 evaluated the signaling profiles of N-terminally FLAG-tagged wild-type (WT) CCR7 using
307 NanoBiT-based G_{i1} dissociation and β-arrestin2 membrane recruitment assays (SI Appendix, Fig.
308 S8A). Given the distinct rotameric states of Y83$^{1.57}$ observed between the two active structures

309 (Fig. 4A,B), we next examined the impact of the Y83$^{1.57}$A mutation on this signaling balance (Fig.
310 4C, D). In response to CCL19, the Y83$^{1.57}$A mutant exhibited reduced potency and efficacy for G_{i1}
311 activation, but maintained potency and elevated efficacy for β-arrestin2 recruitment, despite
312 comparable cell surface expression (SI Appendix, Fig. S8B). Consequently, the Y83$^{1.57}$A mutation
313 shifts the signaling preference toward the β-arrestin2 pathway, suggesting that the Y83$^{1.57}$-
314 mediated conformational transition is critical for transducer selection.

315 Thus, while the core G_i-binding interfaces are highly conserved, our functional data
316 demonstrate that structural variations around the Y83$^{1.57}$ microswitch impact signaling
317 preference. While ICL1 is expected to be flexible due to its lack of direct G protein engagement,
318 the observation of distinct loop conformations even within the static cryo-EM structures
319 highlights the need to investigate the dynamic behavior of the receptor (SI Appendix, Fig. S5C,D
320 and S6). Although ICL1 itself may not be the primary GRK binding site, we hypothesize that the
321 distinct ligand binding modes, relayed via Y83$^{1.57}$, prime the receptor core and intracellular
322 loops to adopt distinct conformational ensembles in the absence of the G protein (42, 43).

323

324 **Molecular dynamics simulations to probe the basis of biased signaling**

325 To investigate how the distinct ligand binding modes and the subtle intracellular
326 differences might influence receptor dynamics relevant to biased signaling, we performed six
327 independent 2.3 µs all-atom MD simulations for each complex (Fig. 5A and SI Appendix, Fig. S9-
328 S12). We used the experimental CCL19- and CCL21-bound structures as starting points,
329 removing the G protein and scFv16 and embedding them in a lipid bilayer to mimic the receptor
330 states primed for subsequent signaling events, such as GRK recruitment (SI Appendix, Fig. S9A).
331 During the simulations, the chemokines exhibited high flexibility, consistent with the cryo-EM
332 densities (SI Appendix, Fig. S3, S4, and S9B,C). Conversely, the receptor 7TM bundles slightly
333 deviated from their initial conformations but converged to similar overall states (SI Appendix,
334 Fig. S9B,C and S10).

335 The most notable finding was the differential dynamics of H8 in CCR7 (Fig. 5A). In the
336 CCL19-bound state, the TM7-H8 loop is highly dynamic, repositioning toward the receptor
337 central axis and widening the gap between TM6 and TM7 (Fig. 5A). This shift is characterized by

338 the approach of the TM7-H8 loop toward TM2 and a pronounced H8 rotation (SI Appendix, Fig.
339 S11). Specifically, the Cα distance between T93$^{2.39}$ and G330$^{8.47}$ narrowed substantially from
340 11.5 Å to 6.4 Å, accompanied by an H8 rotation to a new stable state at -28.2° (relative to the
341 experimental structure, defined as 0°). In contrast, H8 in the CCL21-bound state remained
342 stable near the cryo-EM conformation, with the corresponding Cα distance remaining at 11.3 Å
343 and a less pronounced rotation of -14.4°.

344 These differences trace back to the formation of two distinct salt bridges: a highly stable
345 one directly linking R88$^{12.49}$ (ICL1) to D336$^{8.53}$ (H8) (present in 92% of simulation time), and a
346 second, dynamic one between R88$^{12.49}$ (ICL1) and D94$^{2.40}$ (TM2) (present in 58% of simulation
347 time) (Fig. 5B and SI Appendix, Fig. S12B). In sharp contrast, in the CCL21-bound state, while the
348 R88$^{12.49}$-D336$^{8.53}$ bridge remained largely stable (86% formation), the crucial R88$^{12.49}$-D94$^{2.40}$
349 bridge, which brings H8 toward TM2, was almost entirely absent (9% formation).

350 This dynamic behavior in the CCL19-bound state also correlates with the different chi1
351 (χ1) angles of Y83$^{1.57}$ at the TM1 terminus (180° for CCL19 and -86° for CCL21), observed in the
352 cryo-EM structures, which remained stable in their respective states throughout the
353 simulations (SI Appendix, Fig. S12C). This orientation of Y83$^{1.57}$ appeared to influence the ICL1
354 dynamics and allosteric coupling between ICL1 and H8 (Fig. 5A,B and SI Appendix, Fig. S12D). In
355 the CCL19-bound state, the outward-facing conformation of Y83$^{1.57}$ accommodates F333$^{8.50}$
356 from H8 into a pocket near TM2, whereas the inward-facing Y83$^{1.57}$ in the CCL21-bound state
357 sterically blocks this insertion (SI Appendix, Fig. S12A).

358 Consequently, the stable conformational ensemble induced by CCL21, which lacks deep
359 H8 insertion and resembles the initial G_i-bound conformation, appears suboptimal for GRK
360 interaction. This "locked" state facilitates G protein-biased signaling. Conversely, the
361 conformational flexibility induced by CCL19 allows the receptor to sample multiple states,
362 including a major "open" population characterized by deeper TM7-H8 loop insertion, alongside
363 a population resembling the starting Gi-favorable state. This dynamic equilibrium likely
364 represents the structural basis for CCL19's balanced activation profile, enabling efficient
365 engagement of both effectors.

366

367 **Functional assessment of the dynamic states dictating effector selection**

368 To evaluate this MD-derived dynamic model, we assessed both the G_{i1} and β-arrestin
369 signaling profiles of three structure-guided CCR7 mutants: R88$^{12.49}$A, D94$^{2.40}$A, and D336$^{8.53}$A
370 (Fig. 5C, D). All mutants exhibited cell surface expression levels statistically comparable to WT
371 (SI Appendix, Fig. S8B). Notably, all three mutations significantly and uniformly reduced the
372 maximal efficacy of CCL19-induced β-arrestin2 recruitment (Fig. 5C), highlighting the strict
373 structural requirements for the arrestin-competent state. However, their divergent effects on
374 G_{i1} signaling perfectly encapsulate our dynamic switching model. Similar overall trends were
375 also observed upon CCL21 stimulation (Fig. 5D).

376 The MD simulations indicated that D336$^{8.53}$ serves as a stable resting point for R88$^{12.49}$ in
377 both CCL19- and CCL21-bound states (Fig. 5B). Consistent with the role of D336$^{8.53}$ as a
378 fundamental structural anchor for the receptor's architecture, the D336$^{8.53}$A mutation
379 significantly reduced overall receptor function, demonstrating reduced potency (an increase in
380 the EC_{50}) and a reduction in efficacy for G_{i1} activation, alongside the aforementioned reduction
381 in β-arrestin2 recruitment efficacy (Fig. 5C).

382 Conversely, adopting the GRK-favorable "open" state involves R88$^{12.49}$ dynamically
383 engaging with D94$^{2.40}$ and pulling D336$^{8.53}$ on H8 inward. This transition is highly populated in
384 the balanced CCL19 complex but nearly absent in the G protein-biased CCL21 complex (Fig. 5B).
385 Disrupting this "open-state" tether with the D94$^{2.40}$A mutation resulted in the expected
386 reduction in β-arrestin2 efficacy (Fig. 5C). By limiting the receptor's ability to sample this "open"
387 conformation, the D94$^{2.40}$A mutation appears to favor the "locked" G_i-selective state, thereby
388 maintaining robust WT-level G_{i1} activation despite the targeted loss of β-arrestin2 efficacy.

389 The role of R88$^{12.49}$ in this dynamic mechanism is further supported by the R88$^{12.49}$A
390 mutant. Removing this central basic residue likely impairs the receptor's transition into the
391 D94$^{2.40}$-tethered "open" state, which is consistent with the significant reduction in β-arrestin2
392 efficacy (Fig. 5C). However, its absence does not disrupt the fundamental G_i-binding pocket,
393 allowing the receptor to adopt a G_i-favorable conformation and sustain WT-like G_{i1} activation.
394 Together, these functional data suggest that the dynamic R88$^{12.49}$-mediated network

395 contributes to transducer selection at CCR7, and that the transition required for efficient
396 arrestin engagement depends on this intact basic anchor.
397
398 **Discussion**
399 The precise orchestration of immune cell migration by the CCL19/CCL21-CCR7 axis relies
400 on biased agonism for localized activation versus long-range chemotaxis (22, 26, 27, 44). Here,
401 our structures suggest a molecular framework for this functional divergence. We reveal that
402 ligand recognition is primarily dictated by interactions at the CRS3 interface (Fig. 2). The deep,
403 hydrophobic engagement of the CCL21 30s loop contrasts sharply with the shallower binding of
404 the CCL19 loop, illustrating how the sequence variations in flexible chemokine loops can alter
405 the overall binding topology. Furthermore, our analysis highlights that CCR7 employs a non-
406 canonical, rigid-body movement of TM6 during activation (Fig. 1), likely facilitated by the
407 absence of the canonical $W^{6.48}$ toggle switch, suggesting a specialized adaptation within this
408 receptor subfamily for transducing signals from protein ligands.
409 The central paradox of CCR7 bias is that both ligands induce highly similar G_i-coupled
410 conformations (Fig. 4A,B) yet elicit vastly different downstream responses regarding
411 desensitization (19). Our MD simulations suggest that the mechanism of bias lies not only in the
412 initial G protein engagement, but also in the receptor dynamics that follow G protein
413 dissociation, revealing that CCL19 induces a flexible ensemble capable of adopting a widely
414 "open" H8 state, whereas CCL21 stabilizes a single, "locked" G_i-bound-like state (Fig. 5A).
415 Structural comparisons with GPCR-GRK complexes, such as neurotensin receptor 1
416 (NTSR1) and Rhodopsin (Rho), underscore the importance of this CCL19-induced "open" state
417 (Fig. 6). These structures reveal that the binding modes of the Gα C-terminal α5 helix and the
418 GRK N-terminal α-helix (αN) are mutually exclusive (42, 43, 45, 46) (Fig. 6A, B). While the Gα-α5
419 helix requires deeper insertion towards the receptor core, the GRK-αN helix exhibits a
420 shallower insertion and exits through the lateral gap between TM6 and the TM7-H8 loop. This
421 suggests a general mechanism whereby efficient GRK recognition requires both a sufficiently
422 wide lateral opening and a conformation that disfavors deep G protein re-insertion.

423 In this context, the conformational flexibility of CCL19-bound CCR7 provides a
424 compelling structural rationale for its balanced signaling. Its ability to dynamically adopt the
425 "open" state, where the TM7-H8 loop inserts into the cytoplasmic cavity (Fig. 5A),
426 simultaneously achieves two goals. It sterically hinders deep G protein re-engagement while
427 creating a widened lateral gap favorable for GRK3 engagement (Fig. 6C). Furthermore, this
428 inserted TM7-H8 loop may form a novel composite interaction surface for GRK recognition,
429 analogous to how the GRK-biased small molecule SBI-553 acts on NTSR1 (43). This dynamic
430 equilibrium permits efficient engagement of both effector types. Conversely, the "locked" state
431 stabilized by CCL21 maintains a vacant deep pocket and a narrower lateral gap, rendering it
432 competent for G protein coupling but deficient in the steric opening or interaction surface
433 required for efficient GRK3 engagement. This structural dichotomy offers a mechanistic basis
434 for CCL21's G protein bias.

435 Our mutagenesis data provide functional support for this dynamic model (Fig. 4 and 5),
436 wherein ligand-specific conformations are relayed via the Y83$^{1.57}$ microswitch to govern the
437 intracellular D94$^{2.40}$-R88$^{12.49}$-D336$^{8.53}$ network. Disrupting specific nodes within this network
438 predictably shifts signaling preference: the Y83$^{1.57}$A mutation favors the arrestin pathway,
439 whereas the D94$^{2.40}$A and R88$^{12.49}$A mutations restrict the receptor to a G_i-favorable state.

440 The conceptual framework parallels recent findings in the μ-opioid receptor (μOR),
441 where structural rearrangements narrow the intracellular core to favor arrestin binding over G
442 protein coupling (47). Unlike the concurrent inward shift of TM7 and the TM7-H8 loop in μOR,
443 CCR7 maintains a stable TM7 backbone while its TM7-H8 loop dynamically shifts inward.
444 Pharmacologically, μOR exhibits a pronounced, switch-like shift in signaling bias, whereas CCR7
445 relies on subtle fine-tuning. Despite these differences, both share a fundamental structural
446 principle: partial occupation of the receptor core cavity sterically hinders canonical G protein
447 re-engagement while accommodating the arrestin pathway.

448 Physiologically, CCL19 drives rapid desensitization and internalization suited for acute
449 immune tuning and tissue development (17, 19, 26, 44, 48–51). In contrast, the
450 conformationally restricted ensemble of CCL21 disfavors efficient GRK3 interaction, resulting in
451 sustained G protein signaling essential for long-distance immune cell guidance (17, 22, 28, 49).

452 Moreover, the deep insertion of the CCL21 30s loop may contribute to a slower dissociation
453 rate, further supporting sustained signaling, which, alongside GAG-mediated gradient formation
454 (20–22), explains its role in long-range haptotaxis. In conclusion, this structural and dynamic
455 framework reveals how subtle differences in ligand recognition translate into distinct
456 physiological outcomes. Exploring chemokine analogs that mimic the CRS2/CRS3 engagement
457 profile of CCL21 but at much higher affinity might lead to G protein-biased agonists. Such
458 molecules could promote sustained cell trafficking as adjuvants for vaccines or cancer
459 immunotherapy, providing a foundation for novel immunomodulators.
460

461 **Limitations of Study**

462 While the current study provides significant insights into CCR7 activation and biased signaling
463 mechanisms, several limitations remain. First, our structures do not directly visualize the
464 conformations responsible for GRK or β-arrestin engagement; determining these complex
465 structures will be crucial to fully elucidate the mechanisms of bias. Second, although we
466 observed heterogeneity related to the CCL21 C-terminal tail and potential post-translational
467 modifications, we could not resolve these features at high resolution, warranting further
468 structural investigation. Finally, because of nonspecific activity at 3 µM, CCL21 concentrations
469 in our functional assays were restricted to 1.39 µM. While the G_{i1} assay yielded reliable data
470 within this range, the β-arrestin2 assay did not reach a plateau, precluding the estimation of
471 EC_{50} and maximal responses (E_{max}) and limiting our conclusions regarding CCL21-mediated β-
472 arrestin2 signaling.
473

474 **Materials and Methods**

475 **Mammalian cell culture for recombinant protein production**

476 Expi293F inducible (Expi293Fi) cells (Thermo Fisher Scientific, a component of expression
477 system kit Cat# A39251) were adopted and maintained in HE400AZ media (GMEP)
478 supplemented with 10 µg/mL Blasticidin (InvivoGen) at a 20 mL culture scale. For protein
479 expression, cells were expanded with HE400AZ media up to 200 mL and then HE200 media
480 (GMEP) supplemented with GlutaMAX (Thermo Fisher Scientific) for larger volumes to reduce

481 the total cost. Cells were maintained at a density between 0.3 × 10^6/mL and 4 × 10^6/mL and
482 shaken at 37°C and 130 rpm with 8% (v/v) CO_2. Transfections were performed at a cell density
483 of approximately 3 × 10^6/mL.
484
485 **Insect cell culture for recombinant protein production**
486 For scFv16 expression from *Trichoplusia ni* (Hi5) ovarian cells (Expression Systems, Cat# 94-002),
487 baculovirus was produced in *Spodoptera frugiperda* (Sf9) ovarian cells (ATCC CRL-1711)
488 maintained in Sf-900 III medium (Thermo Fisher Scientific) with 10% (v/v) FBS (Sigma-Aldrich)
489 and 2 mM L-Gln. Hi5 cells were maintained and expanded for protein expression in ESF 921
490 Insect Cell Culture Medium (Expression Systems). Insect cells were grown at 27°C with ambient
491 CO_2 and gentle agitation, and baculovirus infections for virus amplification and protein
492 expression were performed at a cell density of approximately 2 × 10^6/mL.
493
494 **Expression of the apo CCR7-G_i complex**
495 The expression plasmids were designed to perform induced and constitutive co-
496 expression of CCR7 and heterotrimeric G_i protein, and the coding genes were synthesized by
497 GenScript for cloning in expression plasmids. The full-length human CCR7 lacking the
498 endogenous signal peptide (UniProt ID: P32248, residues 25-378) was cloned into pcDNA5/TO
499 vector (Thermo Fisher Scientific) with the N-terminal HA secretion signal peptide followed by a
500 FLAG tag, and a C-terminal LgBiT split NanoLuc fragment (32). Single chain human $G\gamma_2$-$G\alpha_{i1}$,
501 where $G\alpha_{i1}$ (UniProt ID: P63096, residues 2-354) with dominant negative mutations (S47N,
502 G203A, E245A, A326S) (31) was fused downstream of $G\gamma_2$ (UniProt ID: P59768) separated by a
503 3× GSA linker (30) and cloned into the pEG vector (52). Human $G\beta_1$ (UniProt ID: P62873) with C-
504 terminal HiBit NanoLuc complementation fragment and N-terminal 3C protease-cleavable
505 10×His tag was also cloned into the pEG vector for co-expression.
506 Protein expression was performed using Expi293Fi cells as per the manufacturer's
507 recommendation with modifications to use polyethyleneimine (PEI) Max (Polysciences) as a
508 transfection reagent (53), 3 mM sodium valproate and 0.4% (w/v) glucose as enhancers (54),
509 and doxycycline (Wako) as the inducer. The three plasmids were used at an approximately

510 equal weight ratio, and a total of 1 µg plasmid and 4 µg PEI per 1 mL cell culture were mixed in
511 HE400AZ media and incubated for 15 min at room temperature before transfecting the
512 Expi293Fi cells. One day after transfection, the enhancers were added, and after an additional
513 24 hours at 37°C for initial G_i expression, the CCR7 expression was induced by adding 8 µM
514 doxycycline. The culture flask was transferred to a 30°C incubator and shaken for 48 hours. The
515 cells were harvested, washed once with phosphate-buffered saline (PBS), and stored at -30°C.
516 200 mL Expi293Fi culture typically yields approximately 5 grams of cell pellet.
517
518 **Expression and purification of CCL19, CCL21, and scFv16**
519 CCL19 and CCL21 were expressed from Expi293Fi cells but with constitutive expression
520 using a standard CMV promoter, and the coding genes were synthesized by GenScript. Full-
521 length CCL19 (UniProt ID: Q99731) and CCL21 (UniProt ID: O00585) were each fused to the C-
522 terminal 6×His-tagged human IgG1 Fc via the GSGSGSAAA linker, HRV 3C protease site
523 (LEVLFQGP), and GSDGSGSGS linker analogous to the construct previously used to prepare the
524 chemokine domain of CX_3CL1 (55) but cloned into pD649 transient expression vector (ATUM)
525 (56) instead of the BacMam transfer vector (57). Transfection was performed as described for
526 the CCR7-G_i complex with a 1:4 plasmid:PEI ratio, and the enhancers were added to the culture
527 on the following day. The cells were shaken in the 37°C incubator for an additional 84 hours,
528 and the culture supernatant was collected for purification using Ni-NTA (55, 56). The Fc-tagged
529 chemokines were eluted with HEPES-buffered saline (HBS, 10 mM HEPES-Na pH 7.2 and 150
530 mM NaCl) containing 250 mM imidazole, and the Fc tag was removed by adding 2% (w/w) 3C
531 protease, which was prepared in-house. The solutions were buffer exchanged to HBS containing
532 10 mM imidazole, flowed through Ni-NTA equilibrated with HBS containing 20 mM imidazole to
533 remove the Fc tag, and concentrated to approximately 300 µL. Due to the limited protein yields
534 (~50 µM and ~20 µM for CCL19 and CCL21, respectively), the samples were supplemented with
535 10% (v/v) glycerol, aliquoted, flash-frozen, and stored at -80°C for further use.
536 scFv16 (34) was expressed from Hi5 ovarian cells using Bac-to-Bac baculovirus
537 expression system (Thermo Fisher Scientific) and purified as reported previously (55). Briefly,
538 the collected Hi5 culture supernatant was clarified after a precipitate was formed by adding 1

539 mM $NiCl_2$, 5 mM $CaCl_2$, and 50 mM Tris-HCl (pH 8), and then incubated with Ni-NTA to capture
540 the C-terminal 6×His-tagged scFv16. The Ni-NTA resin was collected, washed with HBS
541 containing 20 mM imidazole, and eluted by increasing imidazole concentration to 250 mM. The
542 eluate was concentrated and purified using a size-exclusion chromatography (SEC) column
543 Superdex 75 10/300 GL (Cytiva) equilibrated with HBS. The peak fraction was concentrated to
544 approximately 640 µM, aliquoted and flash-frozen with 10% (v/v) glycerol, and stored at -80°C
545 until future use.
546
547 **Purification of CCR7-G_i-scFv16 complexes bound to CCL19 or CCL21**
548 The ligand-free, NanoBiT-tethered CCR7-G_i-scFv16 complex was purified before the
549 chemokines were added during the final protein concentration step. Approximately 5 grams of
550 cell pellet expressing CCR7-G_i was directly solubilized for 2 hours at 4°C with 10 nmol of
551 recombinant scFv16 and nutation in a solubilization buffer consisting of HBS, 10% (v/v) glycerol,
552 1% (w/v) n-dodecyl-β-D-maltoside (DDM, Anatrace), 0.1% (w/v) lauryl maltose neopentyl glycol
553 (LMNG, Anatrace), 0.11% (w/v) cholesteryl hemisuccinate tris salt (CHS, Anatrace), cOmplete
554 protease inhibitor cocktail (Roche), and apyrase (0.2 µL, New England Biolabs). The resulting
555 cell lysate was clarified by two sequential centrifugations at 12,000 *g* for 30 minutes at 4°C. The
556 supernatant was then supplemented with 3 mM $CaCl_2$ and incubated with 1 mL of in-house
557 anti-FLAG M1 Sepharose for 2 hours at 4°C. The resin was collected in a column and washed
558 sequentially, first with the solubilization buffer, then HBS containing 0.1% LMNG, 0.01% CHS,
559 and 3 mM $CaCl_2$. A final wash was performed with HBS containing 0.01% LMNG, 0.001% CHS,
560 and 3 mM $CaCl_2$, and the CCR7-G_i-scFv16 complex was eluted from the column with HBS buffer
561 containing 0.001% LMNG, 0.001% glyco-diosgenin (GDN, Anatrace), 0.0001% CHS, 5 mM EDTA,
562 and 100 µg/mL FLAG peptide (PH Japan). The eluate was concentrated to approximately 400 µL,
563 and 2% (w/w) of in-house 3C protease was added for overnight incubation at 4°C. The protein
564 was subjected to SEC on a Superdex 200 Increase 10/300 GL column (Cytiva) equilibrated with
565 SEC buffer consisting of HBS, 0.001% LMNG, 0.001% GDN, and 0.0001% CHS. Peak fractions
566 were collected, concentrated, and quantified, yielding approximately 0.20 mg (1.1 nmol) of the
567 purified CCR7-G_i-scFv16 complex.

568 Concurrently, frozen stocks of the chemokines CCL19 and CCL21 were thawed and
569 dialyzed against the SEC buffer using Xpress Micro Dialyzer with a 3.5 kDa molecular weight
570 cutoff (MWCO) (Scienova GmbH). To form the chemokine-bound signaling complexes, each
571 prepared chemokine was added to the purified CCR7-G_i-scFv16 in separate reactions.
572 Specifically, CCL19 was added at a 1.6-fold molar excess to 0.6 nmol of CCR7-G_i-scFv16, while
573 CCL21 was added at the same molar ratio to 0.5 nmol aliquot of the ligand-free complex. Finally,
574 each mixture was concentrated to 4.5 mg/mL using 3 kDa MWCO Amicon Ultra 0.5 mL
575 centrifugal filters for cryo-EM.
576
577 **Cryo-EM grid preparation and data collection**
578 For cryo-EM analysis, a 3.5 µL aliquot of either complex was applied to a glow-
579 discharged Quantifoil R1.2/1.3 300-mesh gold grid. The grids were plunge-frozen in liquid
580 ethane using a Vitrobot Mark IV (Thermo Fisher Scientific) with a 10-sec hold period, blot force
581 of 10, and blotting time of 2-4 sec with 100% humidity at 4°C.
582 Cryo-EM data were subsequently collected using a JEOL JEM-Z320FHC electron
583 microscope operated at 300 kV, equipped with an in-column omega energy filter set to a 20 eV
584 slit width. Images were recorded on a Gatan K3 camera in correlated double sampling mode,
585 with a calibrated pixel size of 0.79 Å at the specimen. Automated data acquisition was
586 performed using SerialEM (58) with a 3 × 3 image-shift pattern and a nominal defocus range of
587 -1.0 to -1.8 µm. Each movie was recorded for 2.6 seconds, fractionated over 50 frames, yielding
588 a total exposure of 50 electrons/$Å^2$ and an exposure rate of 1 electron/$Å^2$ per frame. A total of
589 20,142 movies (7,506 + 12,636) were collected from two grids for the CCL19-CCR7-G_i-scFv16
590 complex, while 5,968 movies (2,376 + 3,592) were collected from two grids for the CCL21-CCR7-
591 G_i-scFv16 complex.
592
593 **Cryo-EM data processing**
594 The data were analyzed using cryoSPARC version 4 (59) for both signaling complexes
595 unless otherwise noted, and the data processing schemes are summarized in SI Appendix, Fig.
596 S3 and S4. Patch motion correction and contrast transfer function (CTF) estimation were

597 performed. Particles were picked iteratively with template-based picking using a representative
598 GPCR-G protein complex and Topaz picking (60) combined with 2D classifications.
599 For the CCL19-CCR7-G_i-scFv16 complex (SI Appendix, Fig. S3), 3,374,958 initial particles
600 were extracted and subjected to Non-uniform Refinement (NU-refine) with Global and Local
601 CTF Refinements. A representative GPCR-G protein-scFv16 complex was used as an initial
602 reference map low-pass filtered to 30 Å. 3D classification was first performed to eliminate the
603 complex particles with poor 7TM density. Several rounds of Heterogeneous Refinement
604 (Hetero-Refine) and NU-Refine were performed to isolate a homogeneous subset of particles.
605 We then utilized 3D Variability Analysis (3DVA) followed by Hetero-Refine using the resulting
606 3DVA volumes as references. While we observed heterogeneity related to glycosylation, such as
607 at N292, we prioritized classes with the best-defined chemokine core features. The resulting
608 class was further refined using Reference-Based Motion Correction (RBMC), NU-refine, and
609 Local CTF Refinement. The selected 256,195 particles were subjected to the final NU-Refine,
610 which yielded a map with a nominal resolution of 3.0 Å as determined by the gold-standard
611 Fourier shell correlation (GSFSC) at the 0.143 threshold.
612 For the CCL21-CCR7-G_i-scFv16 complex (SI Appendix, Fig. S4), 1,537,777 initial particles
613 were processed similarly. After initial 2D and 3D classification, particles representing the best
614 class and minor views from the second-best class were merged and subjected to iterative
615 rounds of NU-Refine, RBMC, and Local CTF-Refine. Subsequent 3DVA-based Hetero-Refine
616 steps were employed to address conformational heterogeneity at the chemokine core. Notably,
617 we identified minor classes exhibiting weak or partial density corresponding to potential N-
618 linked glycosylation at N36 and N292 of CCR7, as well as ambiguous density near the
619 extracellular surface potentially representing parts of the flexible CCL21 C-terminal tail (SI
620 Appendix, Fig. S4A). However, these classes constituted a small fraction of the dataset and
621 displayed lower homogeneity and resolution in the core chemokine-receptor interface
622 compared to the major population. Therefore, we focused on the most homogeneous subset to
623 achieve the highest local resolution (quality or modelability) of the chemokine region. After
624 several rounds of refinement and classification, the final set of 195,011 particles yielded a map
625 with a nominal resolution of 3.2 Å determined by GSFSC at 0.143 threshold.

626 The maps were sharpened with a B-factor of -60 $Å^2$ for model building, refinement and
627 visualization of the map-model correlation. For both datasets, local resolution was estimated
628 using cryoSPARC, and the maps were further sharpened using deepEMhancer for overall map
629 presentation purposes only (61). UCSF pyEM v0.5 (62) was used to plot particle viewing
630 directions on the 3D maps.
631
632 **Model building and refinement**
633 The initial models were prepared using AlphaFold 3 (63), and each subunit was roughly
634 fitted into the map by real-space rigid body refinement using Phenix (64). The models were
635 subjected to iterative rounds of manual rebuilding in Coot (65) and real-space refinement using
636 Phenix. Secondary structure restraints and geometry restraints were applied during refinement.
637 The map-model correlation and refinement statistics are summarized in SI Appendix, Table S1
638 and Fig. S6. Figures were prepared using UCSF ChimeraX (66) and PyMOL (Schrödinger, LLC).
639
640 **Molecular dynamics simulations**
641 Input models and parameters for all-atom MD simulations of CCR7 complexed with
642 CCL19 or CCL21 were generated using CHARMM-GUI (67–69). All molecules other than CCR7
643 and CCL19/21 were stripped from the cryo-EM models. The unmodelled sidechains were
644 manually built and refined with Coot (65). The internal water molecules were placed based on
645 the estimation by HOMOLWAT (70). The unmodelled part of the N-terminus and the C-terminus
646 of CCR7 and CCL19/21 were left unmodelled, and the terminal amino groups and the carboxyl
647 groups were neutrally capped by acetylation (ACE patch) and methylamidation (CT3 patch),
648 respectively. Protonation states of the titratable residues at pH 7.0 were determined with
649 PROPKA (71). The terminal amino groups of the native N-terminus of CCL19 (G1) and CCL21 (S1)
650 were deprotonated by the NGNE and NNEU patches, respectively (estimated pKa 5.96 and 4.51).
651 Because the NGNE patch was not available in CHARMM-GUI, a local install of CHARMM c49b2
652 (72) was used for the patching using the scripts generated by CHARMM-GUI. All the aspartic
653 acid and glutamic acid residues were negatively charged except $D104^{2.50}$ (estimated pKa 7.50 in
654 CCR7-CCL19 and 7.81 in CCR7-CCL21). All the lysine and arginine residues were positively

655 charged. All the histidine residues were neutralized by δ-nitrogen protonation. The model was
656 embedded in a rectangular lipid bilayer comprising 203 POPC molecules (102 in the upper
657 leaflet and 101 in the lower leaflet) with the orientation estimated by PPM2.0 (73). The system
658 was solvated and charge-neutralized by ~24,000 water molecules (water layers of 22.5 Å
659 thickness on top and bottom of the proteins) and 150 mM NaCl. The system dimensions and
660 the total number of atoms were 90 Å × 90 Å × 141 Å and 107,178 atoms for CCL19-CCR7,
661 90 Å × 90 Å × 139 Å and 105,680 atoms for CCL21-CCR7 (SI Appendix, Fig. S9A). The
662 CHARMM36m force-field parameters (74) were used for the proteins, lipids, and ions. The
663 TIP3P model was used for water.

664 MD simulations were performed using GROMACS 2024.3 (75). Each system was energy-
665 minimized using the steepest-descent algorithm for 10,000 steps. Then, six independent MD
666 runs (replicas) were performed. For each replica, the system was equilibrated and relaxed in
667 the following way. First, temperature was elevated from 0 to 100 K for 20 ps in the NVT
668 ensemble using the V-rescale thermostat (76). Temperature was further elevated from 100 K
669 to 310.15 K under the pressure of 1 bar for 400 ps in the NPT ensemble using the V-rescale
670 thermostat and the Berendsen barostat (77). During the energy minimization and the
671 temperature elevation, the x, y, z positions of the backbone heavy atoms, the x, y, z positions of
672 the sidechain heavy atoms, the z positions of the POPC phosphorous atoms, the dihedral angles
673 about the double bond in the POPC alkyl chain, were harmonically restrained to the initial
674 configuration at the force constant of 4000 kJ/mol/nm^2, 2000 kJ/mol/nm^2, 1000 kJ/mol/nm^2
675 and 1000 kJ/mol/rad^2, respectively. Then the restraints were gradually relaxed towards 0 for 35
676 ns in the NPT ensemble of 310.15 K and 1 bar using the V-rescale thermostat and the C-rescale
677 barostat (78). After that, the production run was performed for 2.3 μs in the NPT ensemble of
678 310.15 K and 1 bar using the V-rescale thermostat and the C-rescale barostat at the timestep of
679 2 fs. Bond lengths involving hydrogen atoms were constrained using the LINCS algorithm (79).
680 Long-range electrostatic interactions were calculated with the particle mesh Ewald method (80).
681 Atomic coordinates were saved every 100 ps. The simulations were carried out using the
682 TSUBAME4.0 supercomputer at Institute of Science Tokyo.

683 The molecules were made 'whole' and put back into the simulation cell using the gmx
684 trjconv program in the GROMACS package. The trajectory analysis was performed using
685 MDAnalysis v2.9.0 (81) and the graphs were visualized using Matplotlib (82). To align the
686 trajectories, the corresponding cryo-EM models were used as the alignment references, which
687 were transformed so that the (x, y) origin is the center of the proteins and the z origin is the
688 center of the membrane, and the z-axis is perpendicular to the membrane (SI Appendix, Fig.
689 S10B).

690 In all the trajectory analysis except the ICL1 conformational analysis (SI Appendix, Fig.
691 S12D), the trajectories were least-squares aligned to the reference models by the Cα atoms of
692 CCR7 except the flexible N-terminal (-50) and ECL2 (200-209) regions. In the ICL1
693 conformational analysis (SI Appendix, Fig. S12D), the trajectories were aligned by the Cα atoms
694 of the ICL1-flanking residues of TM1 and TM2 (78-85, 92-99).

695 In all the trajectory analysis except the simulation time course plots, the first 1 μs of the
696 2.3 μs simulation were excluded from the analysis as the relaxation (equilibration) period,
697 because the average RMSD (SI Appendix, Fig. S9B) and the TM displacements (SI Appendix, Fig.
698 S10A) were rapidly changing in this period.

699 The MD snapshots used in the figures were selected so that the TM centroid
700 coordinates and the H8 orientation (the angle and the TM2-G330 distance) are closest to the
701 MD average (the timestep 1597.8 ns of replica #1 for CCL19-CCR7, the timestep 1236.1 ns of
702 replica #1 for CCL21-CCR7).

703 The density plots in Fig. 5A,B and in SI Appendix, Fig. S12A, B were calculated using the
704 Gaussian kernel density estimation implemented in Scikit-learn (83).

705

706 **Plasmids for signaling and expression analysis**

707 The cDNAs encoding full-length human CCR7 (WT) and four point mutants (Y83A, R88A,
708 D94A, and D336A) were chemically synthesized and cloned into the pcDNA3.1(+) vector by
709 GenScript. To facilitate cell surface expression and detection, an HA signal peptide sequence
710 followed by a FLAG epitope tag was genetically fused to the N-terminus of each receptor
711 construct.

712

713 **Cellular CCR7 signaling**

714 ***Cell culture and transfection***

715 HEK293T cells (RIKEN BRC) were seeded at 0.8 × 10^6 cells per well in a 6-well plate for G
716 protein dissociation assay, and 1.6–1.8 × 10^6 cells per 6-cm dish for β-arrestin recruitment assay
717 in Dulbecco's modified Eagle's medium (DMEM, 1 g/L glucose; Wako) supplemented with 10%
718 (v/v) fetal bovine serum (FBS; Sigma-Aldrich), 100 U/mL penicillin, and 100 µg/mL streptomycin
719 (Nacalai Tesque) one day before transfection. Cells were incubated at 37°C in a humidified
720 atmosphere with 5% CO_2.

721 For the NanoBiT G protein dissociation assay, cells were transfected with 200 ng WT or
722 mutant CCR7 in pcDNA3.1, together with 100 ng $G\alpha_{i1}$–LgBiT in pcDNA3.1, 500 ng $G\beta_1$ in
723 pcDNA3.1, 500 ng SmBiT–$G\gamma_2$(C68S) in pCAGGS, and 100 ng Ric8A in pCAGGS. Plasmids were
724 diluted in Opti-MEM I (Thermo Fisher Scientific) and mixed with 5 µg PEI MAX, incubated for 15
725 min at room temperature, and added to the cells.

726 For the NanoBiT β-arrestin recruitment assay, cells were transfected with 400 ng WT or
727 mutant CCR7 in pcDNA3.1, together with 200 ng SmBiT–β-arrestin2 in pCAGGS, and 1 µg LgBiT–
728 CAAX in pCAGGS. Plasmids were diluted in Opti-MEM I and mixed with 10 µg PEI MAX,
729 incubated for 15 min at room temperature, and added to the cells.

730

731 ***NanoBiT G protein dissociation assay***

732 24 hours after transfection, cells were washed with PBS, detached with 0.53 mM EDTA
733 in PBS, diluted with Hank's balanced salt solution (HBSS, pH 7.2; Gibco), and centrifuged at 100
734 × *g* for 3 min. After removal of the supernatant, cells were resuspended in 2 mL of HBSS
735 containing 0.01% (w/v) fatty acid-free bovine serum albumin (BSA; Nacalai Tesque) as assay
736 buffer. The cell suspension was dispensed into a white 384-well plate at 24 µL per well,
737 followed by addition of 6 µL of 50 µM coelenterazine (Selleck Chemicals), diluted in assay buffer.
738 After incubation for 2 h at room temperature, baseline luminescence was recorded using a
739 SpectraMax Mini plate reader (Molecular Devices). Thereafter, 6 µL of 6× ligands prepared in
740 assay buffer were manually added to each well. CCL19 (BioLegend, Cat# 582106) and CCL21

741 (BioLegend, Cat# 582208) were initially prepared at 1 µM and 1.39 µM, respectively, and
742 serially diluted in assay buffer in fivefold steps. The plate was immediately read in kinetic mode,
743 and luminescence counts were recorded for 25 min with an integration time of 0.5 sec per read
744 at 2-min intervals. The luminescence signal remained stable between 8 and 25 min, and data
745 obtained between 10 and 22 min (six time points) were used for analysis.
746
747 ***NanoBiT β-arrestin recruitment assay***
748 24 hours after transfection, cells were harvested as described above, and resuspended
749 in 4 mL of assay buffer. The cell suspension was dispensed into a white 96-well plate at 80 µL
750 per well, followed by addition of 20 µL of 50 µM coelenterazine diluted in assay buffer, and
751 baseline luminescence was recorded. Thereafter, 20 µL of 6× ligands prepared as described
752 above were manually added to each well, and luminescence counts were recorded for 20 min
753 with an integration time of 0.5 sec per read at 1-min intervals. The luminescence signal
754 remained stable between 4 and 20 min, and data obtained between 5 and 12 min (six time
755 points) were used for analysis.
756
757 ***Data analysis***
758 The baseline luminescence recorded prior to ligand addition was used for normalization.
759 For each well, the mean of six consecutive luminescence values within the indicated time
760 window was calculated, and the resulting value was expressed as a fold change relative to the
761 baseline for subsequent analysis. Concentration–response curves were analyzed using Prism 10
762 (GraphPad Software) by nonlinear regression with a variable slope (four-parameter logistic)
763 model. Independent experiments (n = 3) were performed, with WT and mutant receptors
764 analyzed in parallel within each experiment. For each experiment, EC_{50} values and E_{max} of G_{i1}
765 dissociation or β-arrestin2 recruitment were calculated. Statistical comparisons were
766 performed using a paired, two-tailed Student's t-test for WT versus Y83A. For comparisons
767 among WT, R88A, D94A, and D336A, a one-way repeated-measures ANOVA followed by
768 Dunnett's multiple comparisons test (WT vs. each mutant) was applied. A P value < 0.05 was
769 considered statistically significant.

770

771 **Cell surface CCR7 expression**

772 ***Cell culture and transfection***

773 HEK293F cells were maintained in suspension in FreeStyle 293 Expression Medium
774 (Thermo Fisher Scientific) at densities ranging between 0.5×10^6/mL and 2×10^6/mL and shaken
775 at 37°C and 130 rpm with 8% (v/v) CO_2. For transfection, cells were prepared at a density of 1.0
776 $\times 10^6$/mL in a 1 mL volume. Transfection complexes were prepared by mixing 1 µg of plasmid
777 DNA and 4 µg of PEI STAR transfection reagent (Tocris Bioscience) in 100 µL of Opti-MEM
778 (Thermo Fisher Scientific). The mixture was incubated for 10 min at room temperature and
779 added to the cell suspension. The empty pcDNA3.1(+) vector was used as a negative control.
780 Cells were cultured for 24 h prior to analysis.

781

782 ***Flow cytometry***

783 24 hours post-transfection, cells were harvested and washed twice with 1 mL of ice-cold
784 PBE buffer [DPBS (Nacalai Tesque) supplemented with 0.1% BSA and 1 mM EDTA] by
785 centrifugation at 300 × *g* for 3 min at 4°C. The cell pellets were resuspended in 100 µL of PBE
786 buffer containing FITC-conjugated anti-FLAG M2 monoclonal antibody (Sigma-Aldrich, Cat#
787 F4049, 1:100 dilution) and incubated for 1 hour at 4°C. Following incubation, cells were washed
788 twice with 1 mL of PBE and resuspended in 500 µL of the same buffer. The cell surface
789 expression levels were analyzed using a FACSLyric flow cytometer (BD Biosciences). Data
790 collection and analysis were performed using BD FACSuite software. FITC fluorescence was
791 excited by the 488 nm blue laser, separated by a 507 nm long-pass mirror, and detected
792 through a 527/32 nm bandpass filter. A sequential gating strategy was applied to isolate single
793 cells: first, cell debris was excluded based on forward scatter (FSC-A) and side scatter (SSC-A)
794 characteristics. Subsequently, singlets were selected by excluding doublets using FSC-H versus
795 FSC-W and SSC-H versus SSC-W plots. The mean fluorescence intensity (MFI) of the FITC signal
796 in the singlet population was quantified. Statistical analysis was performed on the
797 unnormalized raw MFI data using a one-way ANOVA followed by Dunnett's multiple
798 comparisons test against the WT group in Prism 8 (GraphPad Software).

References

1. D. J. Fowell, M. Kim, The spatio-temporal control of effector T cell migration. *Nat. Rev. Immunol.* **21**, 582–596 (2021).
2. H. Qi, W. Kastenmüller, R. N. Germain, Spatiotemporal basis of innate and adaptive immunity in secondary lymphoid tissue. *Annu. Rev. Cell Dev. Biol.* **30**, 141–167 (2014).
3. M. D. Gunn, *et al.*, Mice lacking expression of secondary lymphoid organ chemokine have defects in lymphocyte homing and dendritic cell localization. *J. Exp. Med.* **189**, 451–460 (1999).
4. R. Förster, *et al.*, CCR7 coordinates the primary immune response by establishing functional microenvironments in secondary lymphoid organs. *Cell* **99**, 23–33 (1999).
5. K. Reif, *et al.*, Balanced responsiveness to chemoattractants from adjacent zones determines B-cell position. *Nature* **416**, 94–99 (2002).
6. A. J. Ozga, M. T. Chow, A. D. Luster, Chemokines and the immune response to cancer. *Immunity* **54**, 859 (2021).
7. M. Birkenbach, K. Josefsen, R. Yalamanchili, G. Lenoir, E. Kieff, Epstein-Barr virus-induced genes: first lymphocyte-specific G protein-coupled peptide receptors. *J. Virol.* **67**, 2209–20 (1993).
8. R. Yoshida, *et al.*, Molecular cloning of a novel human CC chemokine EBI1-ligand chemokine that is a specific functional ligand for EBI1, CCR7. *Journal of Biological Chemistry* **272**, 13803–13809 (1997).
9. M. Nagira, *et al.*, Molecular cloning of a novel human cc chemokine secondary lymphoid- tissue chemokine that is a potent chemoattractant for lymphocytes and mapped to chromosome 9p13. *Journal of Biological Chemistry* **272**, 19518–19524 (1997).
10. R. Förster, A. C. Davalos-Misslitz, A. Rot, CCR7 and its ligands: balancing immunity and tolerance. *Nat. Rev. Immunol.* **8**, 362–371 (2008).
11. I. Comerford, *et al.*, A myriad of functions and complex regulation of the CCR7/CCL19/CCL21 chemokine axis in the adaptive immune system. *Cytokine Growth Factor Rev.* **24**, 269–283 (2013).
12. S. A. Luther, H. L. Tang, P. L. Hyman, A. G. Farr, J. G. Cyster, Coexpression of the chemokines ELC and SLC by T zone stromal cells and deletion of the ELC gene in the plt/plt mouse. *Proc. Natl. Acad. Sci. U. S. A.* **97**, 12694–12699 (2000).
13. L. Han, L. Zhang, CCL21/CCR7 axis as a therapeutic target for autoimmune diseases. *Int. Immunopharmacol.* **121**, 110431 (2023).
14. A. Salem, M. Alotaibi, R. Mroueh, H. A. Basheer, K. Afarinkia, CCR7 as a therapeutic target in Cancer. *Biochim. Biophys. Acta Rev. Cancer* **1875**, 188499 (2021).
15. K. Jaeger, *et al.*, Structural Basis for Allosteric Ligand Recognition in the Human CC Chemokine Receptor 7. *Cell* **178**, 1222-1230.e10 (2019).

840 16. M. A. Hauser, D. F. Legler, Common and biased signaling pathways of the
841 chemokine receptor CCR7 elicited by its ligands CCL19 and CCL21 in leukocytes. *J.*
842 *Leukoc. Biol.* **99**, 869–882 (2016).
843 17. T. A. Kohout, *et al.*, Differential desensitization, receptor phosphorylation, β-
844 arrestin recruitment, and ERK1/2 activation by the two endogenous ligands for the
845 CC chemokine receptor 7. *Journal of Biological Chemistry* **279**, 23214–23222
846 (2004).
847 18. M. A. Byers, *et al.*, Arrestin 3 mediates endocytosis of CCR7 following ligation of
848 CCL19 but not CCL21. *J. Immunol.* **181**, 4723–4732 (2008).
849 19. D. A. Zidar, J. D. Violin, E. J. Whalen, R. J. Lefkowitz, Selective engagement of G
850 protein coupled receptor kinases (GRKs) encodes distinct functions of biased
851 ligands. *Proc. Natl. Acad. Sci. U. S. A.* **106**, 9649–9654 (2009).
852 20. G. M. Hjortø, *et al.*, Differential CCR7 targeting in dendritic cells by three naturally
853 occurring CC-chemokines. *Front. Immunol.* **7**, 218657 (2016).
854 21. K. Schumann, *et al.*, immobilized chemokine fields and soluble chemokine
855 gradients cooperatively shape migration patterns of dendritic cells. *Immunity* **32**,
856 703–713 (2010).
857 22. M. Weber, *et al.*, Interstitial dendritic cell guidance by haptotactic chemokine
858 gradients. *Science* **339**, 328–332 (2013).
859 23. M. Leick, *et al.*, CCL19 is a specific ligand of the constitutively recycling atypical
860 human chemokine receptor CRAM-B. *Immunology* **129**, 536–546 (2010).
861 24. M. H. Ulvmar, *et al.*, The atypical chemokine receptor CCRL1 shapes functional
862 CCL21 gradients in lymph nodes. *Nat. Immunol.* **15**, 623–630 (2014).
863 25. S. A. Bryce, *et al.*, ACKR4 on Stromal Cells Scavenges CCL19 To Enable CCR7-
864 Dependent Trafficking of APCs from Inflamed Skin to Lymph Nodes. *J. Immunol.*
865 **196**, 3341–3353 (2016).
866 26. Y. Yanagawa, K. Onoé, CCL19 induces rapid dendritic extension of murine dendritic
867 cells. *Blood* **100**, 1948–1956 (2002).
868 27. S. A. Luther, *et al.*, Differing activities of homeostatic chemokines CCL19, CCL21,
869 and CXCL12 in lymphocyte and dendritic cell recruitment and lymphoid neogenesis.
870 *J. Immunol.* **169**, 424–433 (2002).
871 28. Ulrike Haessler, Marco Pisano, Mingming Wu, M. A. Swartz, Dendritic cell
872 chemotaxis in 3D under defined chemokine gradients reveals differential response
873 to ligands CCL21 and CCL19. *Proc. Natl. Acad. Sci. U. S. A.* **108**, 5614–5619 (2011).
874 29. A. S. Jørgensen, M. M. Rosenkilde, G. M. Hjortø, Biased signaling of G protein-
875 coupled receptors – From a chemokine receptor CCR7 perspective. *Gen. Comp.*
876 *Endocrinol.* **258**, 4–14 (2018).
877 30. X. Barros-Álvarez, *et al.*, The tethered peptide activation mechanism of adhesion
878 GPCRs. *Nature* **604**, 757–762 (2022).
879 31. Y. L. Liang, *et al.*, Dominant Negative G Proteins Enhance Formation and
880 Purification of Agonist-GPCR-G Protein Complexes for Structure Determination.
881 *ACS Pharmacol. Transl. Sci.* **1**, 12–20 (2018).
882 32. A. S. Dixon, *et al.*, NanoLuc Complementation Reporter Optimized for Accurate
883 Measurement of Protein Interactions in Cells. *ACS Chem. Biol.* **11**, 400–8 (2016).

884 33. J. Duan, *et al.*, Cryo-EM structure of an activated VIP1 receptor-G protein complex
885 revealed by a NanoBiT tethering strategy. *Nat. Commun.* **11**, 4121 (2020).
886 34. S. Maeda, *et al.*, Development of an antibody fragment that stabilizes GPCR/G-
887 protein complexes. *Nat. Commun.* **9**, 3712 (2018).
888 35. Z. Shao, *et al.*, Molecular insights into ligand recognition and activation of
889 chemokine receptors CCR2 and CCR3. *Cell Discov.* **8**, 44 (2022).
890 36. K. Liu, *et al.*, Structural basis of CXC chemokine receptor 2 activation and signalling.
891 *Nature* **585**, 135–140 (2020).
892 37. D. J. Wasilko, *et al.*, Structural basis for CCR6 modulation by allosteric antagonists.
893 *Nat. Commun.* **15**, 7574 (2024).
894 38. Q. Zhou, *et al.*, Common activation mechanism of class A GPCRs. *Elife* **8** (2019).
895 39. L. Urvas, E. Kellenberger, Structural Insights into Molecular Recognition and
896 Receptor Activation in Chemokine-Chemokine Receptor Complexes. *J. Med. Chem.*
897 **66**, 7070–7085 (2023).
898 40. M. M. Rosenkilde, T. Benned-Jensen, T. M. Frimurer, T. W. Schwartz, The minor
899 binding pocket: A major player in 7TM receptor activation. *Trends Pharmacol. Sci.*
900 **31**, 567–574 (2010).
901 41. A. S. Jørgensen, *et al.*, Biased Signaling of CCL21 and CCL19 Does Not Rely on N-
902 Terminal Differences, but Markedly on the Chemokine Core Domains and
903 Extracellular Loop 2 of CCR7. *Front. Immunol.* **10**, 2156 (2019).
904 42. Q. Chen, *et al.*, Structures of rhodopsin in complex with G-protein-coupled
905 receptor kinase 1. *Nature* **595**, 600–605 (2021).
906 43. J. Duan, *et al.*, GPCR activation and GRK2 assembly by a biased intracellular agonist.
907 *Nature* **620**, 676–681 (2023).
908 44. A. Link, *et al.*, Fibroblastic reticular cells in lymph nodes regulate the homeostasis
909 of naive T cells. *Nat. Immunol.* **8**, 1255–1265 (2007).
910 45. H. E. Kato, *et al.*, Conformational transitions of a neurotensin receptor 1-Gi1
911 complex. *Nature* **572**, 80–85 (2019).
912 46. Y. Gao, *et al.*, Structures of the Rhodopsin-Transducin Complex: Insights into G-
913 Protein Activation. *Mol. Cell* **75**, 781-790.e3 (2019).
914 47. Q. Qu, *et al.*, Insights into distinct signaling profiles of the μOR activated by diverse
915 agonists. *Nat. Chem. Biol.* **19**, 423–430 (2023).
916 48. M. R. Britschgi, A. Link, T. K. A. Lissandrin, S. A. Luther, Dynamic modulation of
917 CCR7 expression and function on naive T lymphocytes in vivo. *J. Immunol.* **181**,
918 7681–7688 (2008).
919 49. S. Nandagopal, D. Wu, F. Lin, Combinatorial guidance by CCR7 ligands for T
920 lymphocytes migration in co-existing chemokine fields. *PLoS One* **6**, e18183 (2011).
921 50. K. Schaeuble, *et al.*, Perivascular Fibroblasts of the Developing Spleen Act as
922 LTα1β2-Dependent Precursors of Both T and B Zone Organizer Cells. *Cell Rep.* **21**,
923 2500–2514 (2017).
924 51. K. Y. Chen, *et al.*, Inflammation switches the chemoattractant requirements for
925 naive lymphocyte entry into lymph nodes. *Cell* **188**, 1019-1035.e22 (2025).
926 52. A. Goehring, *et al.*, Screening and large-scale expression of membrane proteins in
927 mammalian cells for structural studies. *Nat. Protoc.* **9**, 2574–2585 (2014).

928 53. P. A. Longo, J. M. Kavran, M.-S. Kim, D. J. Leahy, Transient mammalian cell
929 transfection with polyethylenimine (PEI). *Methods Enzymol.* **529**, 227–40 (2013).
930 54. A. Wellner, *et al.*, Rapid generation of potent antibodies by autonomous
931 hypermutation in yeast. *Nat. Chem. Biol.* **17**, 1057–1064 (2021).
932 55. N. Tsutsumi, *et al.*, Atypical structural snapshots of human cytomegalovirus GPCR
933 interactions with host G proteins. *Sci. Adv.* **8**, eabl5442 (2022).
934 56. N. Tsutsumi, *et al.*, Structure of the thrombopoietin-MPL receptor complex is a
935 blueprint for biasing hematopoiesis. *Cell* **186**, 4189-4203.e22 (2023).
936 57. A. Dukkipati, H. H. Park, D. Waghray, S. Fischer, K. C. Garcia, BacMam system for
937 high-level expression of recombinant soluble and membrane glycoproteins for
938 structural studies. *Protein Expr. Purif.* **62**, 160–170 (2008).
939 58. M. Schorb, I. Haberbosch, W. J. H. Hagen, Y. Schwab, D. N. Mastronarde, Software
940 tools for automated transmission electron microscopy. *Nat. Methods* **16**, 471–477
941 (2019).
942 59. A. Punjani, J. L. Rubinstein, D. J. Fleet, M. A. Brubaker, cryoSPARC: algorithms for
943 rapid unsupervised cryo-EM structure determination. *Nat. Methods* **14**, 290–296
944 (2017).
945 60. T. Bepler, *et al.*, Positive-unlabeled convolutional neural networks for particle
946 picking in cryo-electron micrographs. *Nat. Methods* **16**, 1153–1160 (2019).
947 61. R. Sanchez-Garcia, *et al.*, DeepEMhancer: a deep learning solution for cryo-EM
948 volume post-processing. *Commun. Biol.* **4**, 874 (2021).
949 62. D. Asarnow, E. Palovcak, Y. Cheng, asarnow/pyem: UCSF pyem v0.5. [Preprint]
950 (2019). Available at: https://doi.org/10.5281/zenodo.3576630.
951 63. J. Abramson, *et al.*, Accurate structure prediction of biomolecular interactions with
952 AlphaFold 3. *Nature* **630**, 493–500 (2024).
953 64. D. Liebschner, *et al.*, Macromolecular structure determination using X-rays,
954 neutrons and electrons: recent developments in Phenix. *Acta Crystallogr. D Struct.*
955 *Biol.* **75**, 861–877 (2019).
956 65. P. Emsley, B. Lohkamp, W. G. Scott, K. Cowtan, Features and development of Coot.
957 *Acta Crystallogr. D Biol. Crystallogr.* **66**, 486–501 (2010).
958 66. E. F. Pettersen, *et al.*, UCSF ChimeraX: Structure visualization for researchers,
959 educators, and developers. *Protein Sci.* **30**, 70–82 (2021).
960 67. S. Jo, T. Kim, V. G. Iyer, W. Im, CHARMM-GUI: a web-based graphical user interface
961 for CHARMM. *J. Comput. Chem.* **29**, 1859–1865 (2008).
962 68. J. Lee, *et al.*, CHARMM-GUI Input Generator for NAMD, GROMACS, AMBER,
963 OpenMM, and CHARMM/OpenMM Simulations Using the CHARMM36 Additive
964 Force Field. *J. Chem. Theory Comput.* **12**, 405–413 (2016).
965 69. E. L. Wu, *et al.*, CHARMM-GUI Membrane Builder toward realistic biological
966 membrane simulations. *J. Comput. Chem.* **35**, 1997–2004 (2014).
967 70. E. Mayol, *et al.*, HomolWat: a web server tool to incorporate "homologous" water
968 molecules into GPCR structures. *Nucleic Acids Res.* **48**, W54–W59 (2020).
969 71. D. C. Bas, D. M. Rogers, J. H. Jensen, Very fast prediction and rationalization of pKa
970 values for protein-ligand complexes. *Proteins* **73**, 765–783 (2008).

72. B. R. Brooks, *et al.*, CHARMM: the biomolecular simulation program. *J. Comput. Chem.* **30**, 1545–1614 (2009).
73. M. A. Lomize, I. D. Pogozheva, H. Joo, H. I. Mosberg, A. L. Lomize, OPM database and PPM web server: resources for positioning of proteins in membranes. *Nucleic Acids Res.* **40**, D370-6 (2012).
74. J. Huang, *et al.*, CHARMM36m: an improved force field for folded and intrinsically disordered proteins. *Nat. Methods* **14**, 71–73 (2017).
75. D. Van Der Spoel, *et al.*, GROMACS: fast, flexible, and free. *J. Comput. Chem.* **26**, 1701–1718 (2005).
76. G. Bussi, D. Donadio, M. Parrinello, Canonical sampling through velocity rescaling. *J. Chem. Phys.* **126**, 014101 (2007).
77. H. J. C. Berendsen, J. P. M. Postma, W. F. Van Gunsteren, A. Dinola, J. R. Haak, Molecular dynamics with coupling to an external bath. *J. Chem. Phys.* **81**, 3684–3690 (1984).
78. M. Bernetti, G. Bussi, Pressure control using stochastic cell rescaling. *J. Chem. Phys.* **153**, 114107 (2020).
79. B. Hess, P-LINCS: A Parallel Linear Constraint Solver for Molecular Simulation. *J. Chem. Theory Comput.* **4**, 116–122 (2008).
80. T. Darden, D. York, L. Pedersen, Particle mesh Ewald: An N·log(N) method for Ewald sums in large systems. *J. Chem. Phys.* **98**, 10089–10092 (1993).
81. N. Michaud-Agrawal, E. J. Denning, T. B. Woolf, O. Beckstein, MDAnalysis: a toolkit for the analysis of molecular dynamics simulations. *J. Comput. Chem.* **32**, 2319–2327 (2011).
82. J. D. Hunter, Matplotlib: A 2D graphics environment. *Comput. Sci. Eng.* **9**, 90–95 (2007).
83. F. Pedregosa, *et al.*, Scikit-learn: Machine Learning in Python. *Journal of Machine Learning Research* **12**, 2825–2830 (2011).

1000 **Data, Materials, and Software Availability**

1001 The cryo-EM maps and the corresponding atomic coordinates have been deposited in the
1002 Electron Microscopy Data Bank (EMDB) and the Protein Data Bank (PDB) under accession codes
1003 EMD-66874 (PDB: 9XHH) and EMD-66875 (PDB: 9XHI) for CCL19-CCR7-G_i-scFv16 and CCL21-
1004 CCR7-G_i-scFv16, respectively. The MD simulation trajectories generated in this study are
1005 available at Zenodo [https://doi.org/10.5281/zenodo.18859194]. Any additional information
1006 required to reanalyze the data reported in this paper, as well as unique and stable reagents
1007 generated in this study, are available from the corresponding author upon reasonable request.

1008

1009 **Acknowledgements**

1010 We thank Gaku Nakamura and Dr. Asuka Inoue for providing the NanoBiT assay plasmids and
1011 technical guidance. We also thank the members of the Cellular and Structural Physiology
1012 Laboratory (CeSPL) for their daily scientific discussions, and Ms. Miho Sasaki for her research
1013 support. We used Google Gemini (Gemini 3.1 Pro) to edit the text and enhance readability,
1014 maintaining full oversight, fact-checking all outputs, and taking full accountability for the final
1015 content. This work was supported by the Japan Society for the Promotion of Science (JSPS)
1016 KAKENHI (grant numbers JP24K01965 and JP24K21935 to N.T., and JP20H00451 to Y.F.), the
1017 Kobayashi Foundation (grant number 303 to Y.S.), and the Kurume University Ishibashi
1018 Foundation for the Promotion of Science (to Y.S.). The MD simulations were performed using
1019 the TSUBAME4.0 supercomputer at the Institute of Science Tokyo.

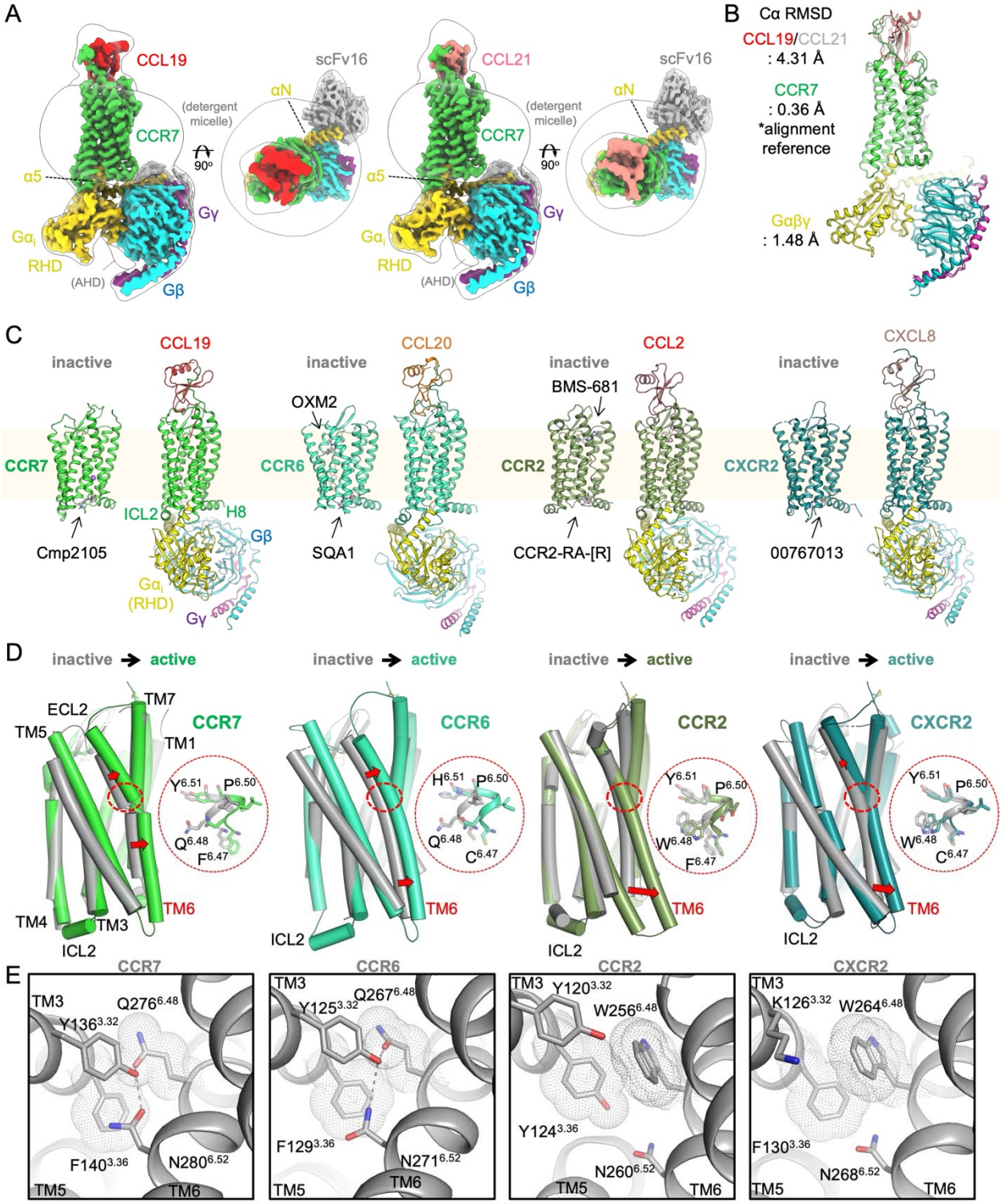

Fig. 1 | Structures of CCR7-G_i complexes and global conformational changes upon activation. (A) Cryo-EM maps of the CCL19-CCR7-G_i-scFv16 (left) and CCL21-CCR7-G_i-scFv16 (right) complexes. Structures are shown in side views and top views. Color coding: CCL19 (red), CCL21 (orange), CCR7 (green), $G\alpha_i$ (yellow; RHD: Ras Homology Domain, AHD: Alpha Helical Domain), Gβ (cyan), Gγ (purple), scFv16 (gray). (B) Superposition of the ribbon models of the CCL19-

1026 bound and CCL21-bound complexes. Alignment was performed based on CCR7. Cα root-mean-
1027 square deviations (RMSD) are indicated for the chemokines, CCR7, and Gαβγ. (C) Comparison of
1028 active and inactive state structures of CCR7 and related chemokine receptors. Overall
1029 structures showing G protein coupling or antagonist/inhibitor binding. Structures include
1030 inactive CCR7 bound to Cmp2105 (PDB: 6QZH); active CCR7 bound to CCL19 (this study);
1031 inactive CCR6 bound to OXM2 and SQA1 (PDB: 9D3E); active CCR6 bound to CCL20 (PDB:
1032 6WWZ); inactive CCR2 bound to BMS-681 and CCR2-RA-[R] (PDB: 5T1A); active CCR2 bound to
1033 CCL2 (PDB: 7XA3); inactive CXCR2 bound to 00767013 (PDB: 6LFL); active CXCR2 bound to
1034 CXCL8 (PDB: 6LFO). (D) Superposition of the inactive and active structures of chemokine
1035 receptors. Inactive states are shown in gray, and active states are separately colored. Red
1036 arrows indicate the outward movement of TM6. The region corresponding to the conserved
1037 CWxP motif (FQxP in CCR7 and CCR6) is indicated by red dashed circles and shown on the right.
1038 (E) Structural comparison of the inactive-state chemokine receptors viewed from the
1039 extracellular side. Key residues around position 6.48 are shown as sticks, and the $F/Y^{3.36}$ and
1040 $Q/W^{6.48}$ sidechains are displayed with dot surfaces to illustrate their steric bulk. Hydrogen-
1041 bonding networks are indicated by dashed lines.

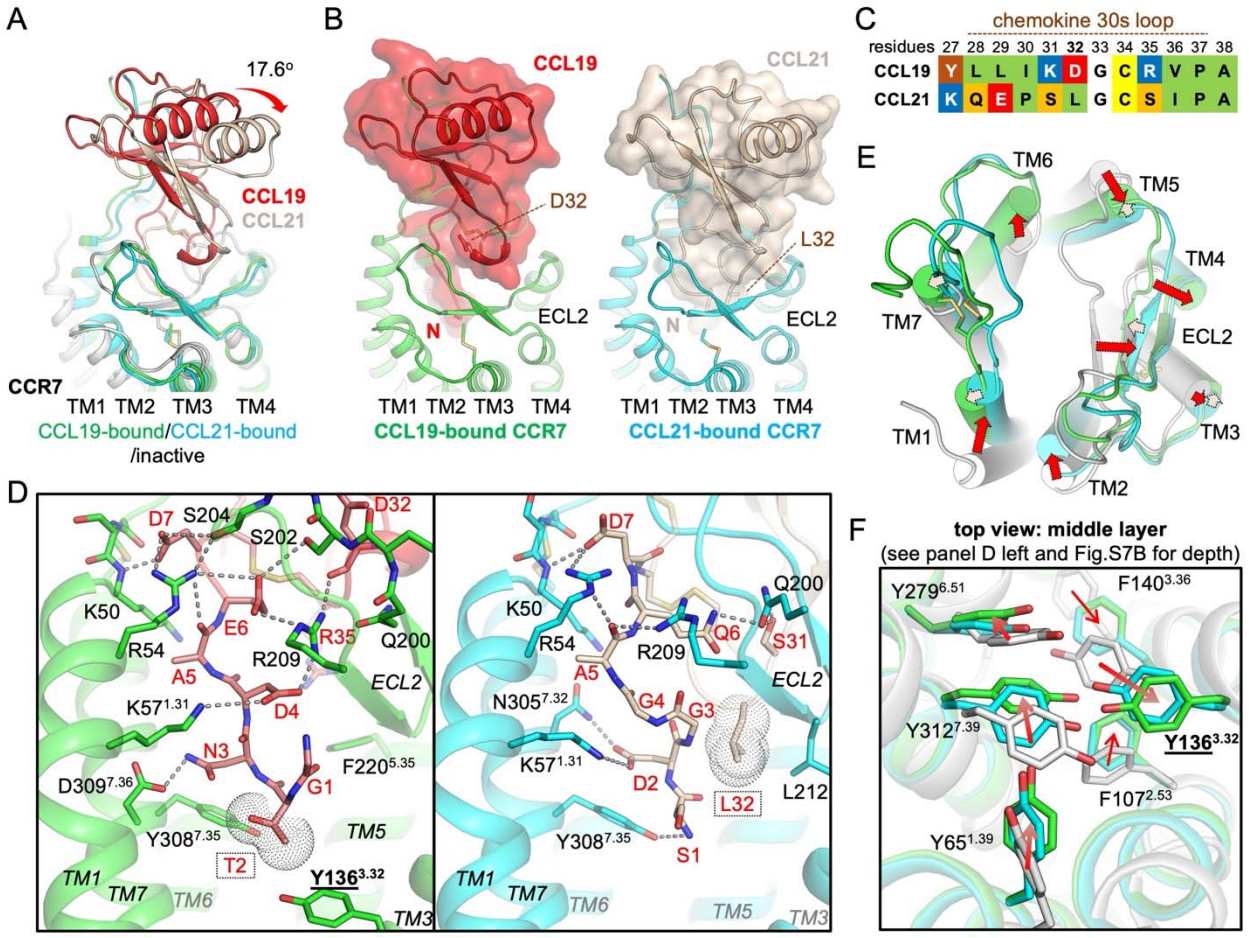

Fig. 2 | Distinct ligand binding modes of CCL19 and CCL21 at CCR7.
(A) Superposition of the CCL19-CCR7 (red/green) and CCL21-CCR7 (orange/cyan) complexes with inactive CCR7 (gray), highlighting the 17.6° rotation of CCL21 relative to CCL19. (B) Divergent interactions at the CRS3 interface. CCL19-CCR7 (left) and CCL21-CCR7 (right) are shown side-by-side to compare the extracellular structures especially the interaction between the chemokine 30s loop and CCR7-ECL2 at CRS3. The central residues in the 30s loop (D32 for CCL19 and L32 for CCL21) are indicated as markers. (C) A sequence alignment of the 30s loops of CCL19 and CCL21. (D) Conserved and distinct interactions at the CRS2/3 interfaces. Close-up views of the chemokine N-terminus penetration into the orthosteric binding pocket for CCL19 (left) and CCL21 (right). Key interacting residues are shown as sticks, and polar interactions are indicated by dashed lines. (E) Ligand-specific conformational changes in the extracellular TMs and ECL2. Superposition of the CCL19-bound and CCL21-bound CCR7 structures with the inactive CCR7 structure, highlighting the conformational differences induced by the distinct ligand binding modes. Red arrows indicate conformational shifts from the inactive state to the CCL21-bound state, and peach arrows indicate the further shifts observed in the CCL19-bound state. (F) Rearrangement of the aromatic cluster in the middle layer of the TM bundle. Close-up view of the superimposed structures showing the distinct conformations of Y65$^{1.39}$, F107$^{2.53}$, Y136$^{3.32}$, Y279$^{6.51}$, Y308$^{7.35}$, and Y312$^{7.39}$ in the CCL19-bound and CCL21-bound states compared to the inactive CCR7 (PDB: 6QZH). See also Fig. S7.

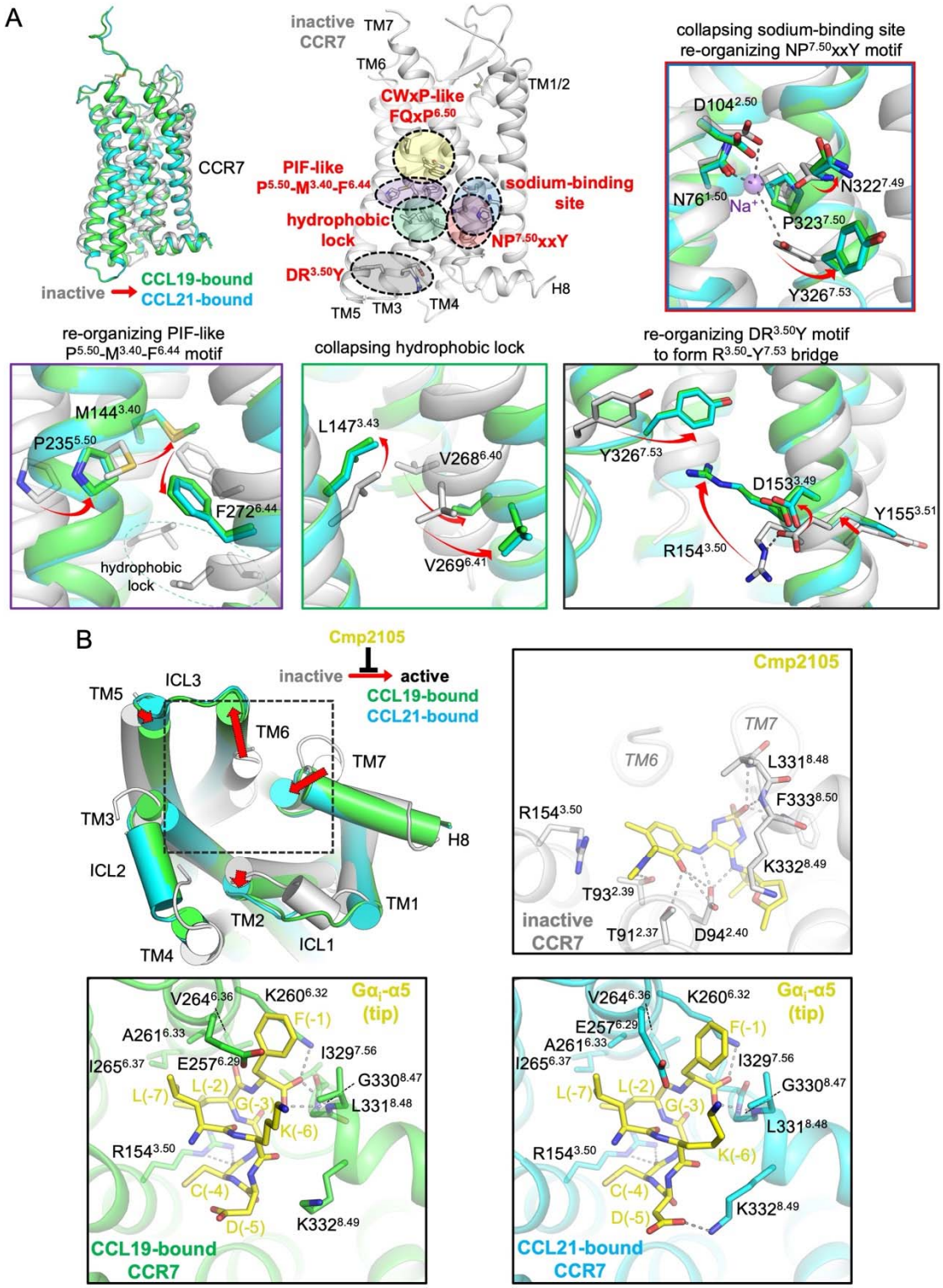

Fig. 3 | Structural basis of CCR7 activation.

(A) Conserved GPCR activation motifs and conformational changes in CCR7. Top left: Superposition of inactive CCR7 (gray) and active CCR7 (CCL19-bound in green, CCL21-bound in cyan). Top center: Mapping of the key GPCR activation motifs highlighted on the inactive CCR7

1067 structure. Other panels show close-up views of the reorganization of the motifs upon activation.
1068 Key residues are shown as sticks. Arrows indicate the direction of movement from the inactive
1069 to the active state. Top right: Collapse of the sodium-binding site and reorganization of the
1070 $NP^{7.50}$xxY motif. Bottom left: Reorganization of the PIF-like $P^{5.50}$-$M^{3.40}$-$F^{6.44}$ motif upstream of
1071 the hydrophobic lock. Bottom center: Collapse of the hydrophobic lock. Bottom right:
1072 Reorganization of the $DR^{3.50}$Y motif and formation of a G protein-binding interface with the
1073 $R^{3.50}$-$Y^{7.53}$ bridge. (B) G protein coupling and comparison with the antagonist-bound state. Top
1074 left: Superposition of active CCR7 (CCL19-bound in green, CCL21-bound in cyan) and inactive
1075 CCR7 bound to Cmp2105 (gray). The inactive-to-active TM movements, which are generally
1076 conserved between the CCL19-bound and CCL21-bound states in complex with G_i, are indicated
1077 by red arrows. Top right: Close-up view showing how Cmp2105 (yellow sticks) occupies the G
1078 protein binding site in the inactive CCR7. Cmp2105 also inhibits the inactive-to-active
1079 conformational transition. Bottom panels: Detailed interactions between the $G\alpha_i$ α5 helix
1080 (yellow, C-terminal 7 residues) and the CCR7 intracellular cavity in the CCL19-bound (left) and
1081 CCL21-bound (right) complexes. Key residues involved in the interaction are shown as sticks,
1082 and polar contacts are indicated by dashed lines.

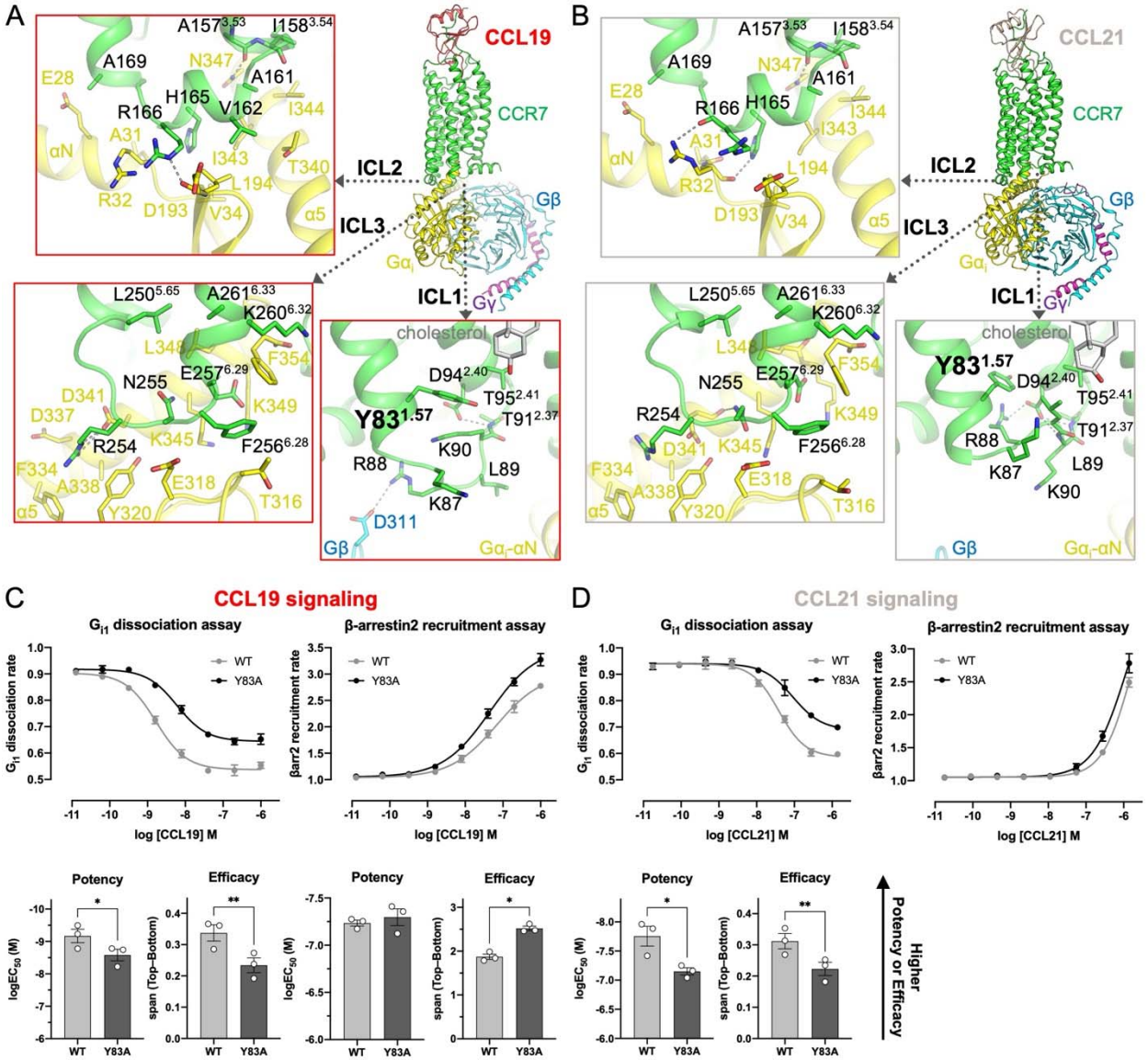

Fig. 4 | Conserved G_i interface with distinct Y83 rotameric states.
The G_i binding interface of the (A) CCL19-CCR7-G_i and (B) CCL21-CCR7-G_i complexes. Overall views are displayed on top right, where zoomed-in boxes highlight the interfaces centering around ICL2 (top left), ICL3 (bottom left), and ICL1 (bottom right). The contacting residues within 4 Å distance are shown as sticks, and polar interactions are shown by dashed lines. Cholesterol molecules near ICL1 are shown as gray sticks. (C,D) Effects of the Y83A mutation on G_{i1} and β-arrestin2 signaling induced by CCL19 and CCL21. G_{i1} dissociation and β-arrestin2 recruitment in response to (C) CCL19 or (D) CCL21 at WT and Y83A CCR7. Representative concentration-response curves are shown in the top panels, while potency ($logEC_{50}$) and efficacy (span; Top-Bottom) are presented as bar graphs in the bottom panels. Because a clear plateau was not achieved for β-arrestin2 recruitment in response to CCL21, $logEC_{50}$ and span values could not be reliably estimated and are therefore not determined. Concentration-response curves represent a single experiment performed in triplicate and are shown as mean ± standard deviation (SD). Summary data represent three independent experiments and are

1098 shown as mean ± standard error of the mean (SEM). Statistical comparisons between WT and
1099 Y83A were performed using paired two-tailed t-tests (* $P < 0.05$; ** $P < 0.01$). βarr2, β-arrestin2.

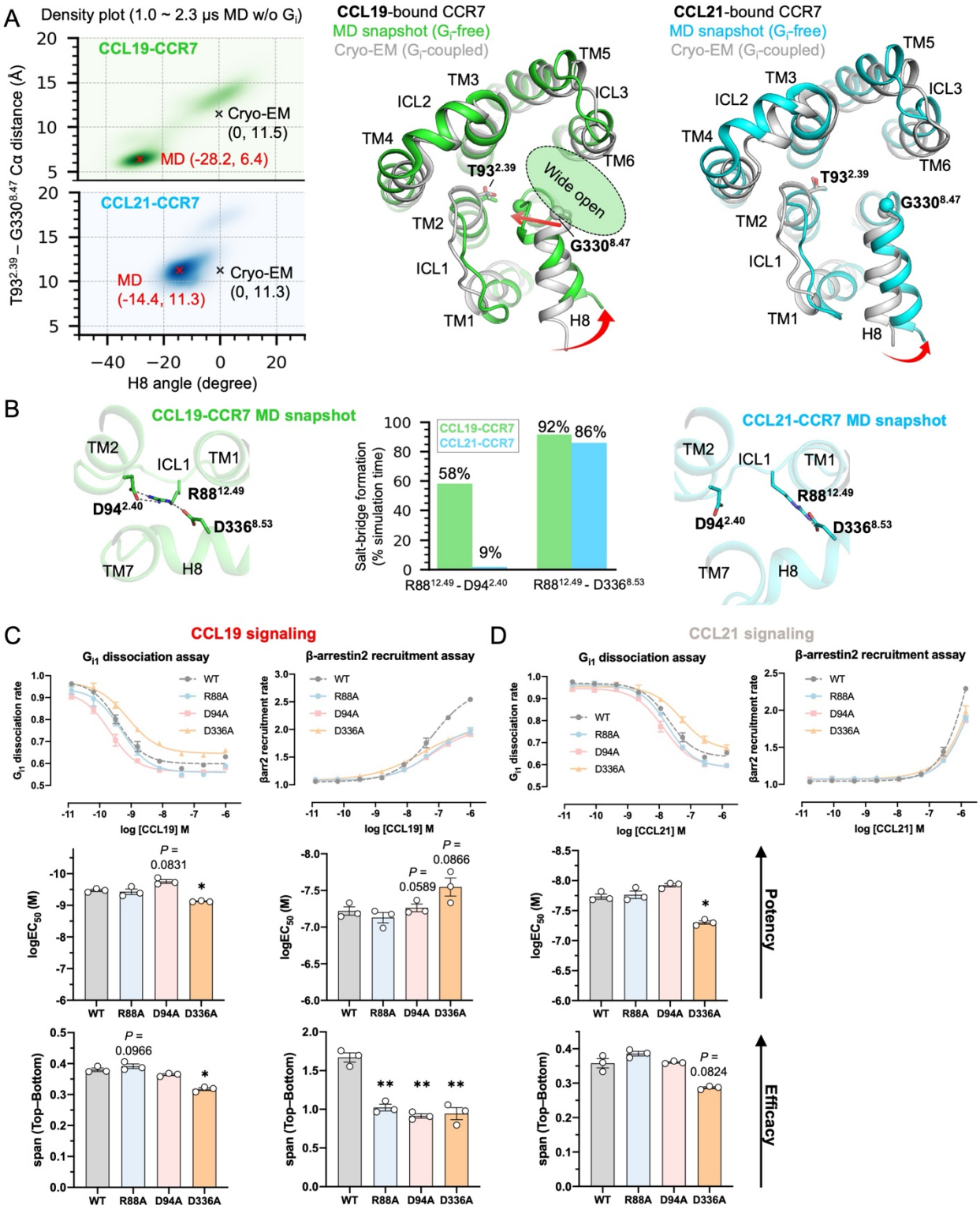

Fig. 5 | Distinct intracellular dynamics revealed by MD simulations and functional validation. (A) Comparison of the H8 orientation after the G_i free MD simulations between CCL19-bound (green) and CCL21-bound (cyan) CCR7. Left: Probability density plot of the H8 angle versus the $T93^{2.39}$-$G330^{8.47}$ distance. Data were calculated from six independent 2.3 μs G_i-free MD simulations, excluding the first 1 μs of each run as a relaxation period. See Fig. S11C for the

1106 definition of the H8 angle. The angles and the distances from the cryo-EM models and the MD
1107 density peak are indicated by black and red crosses ('x') with corresponding text, respectively.
1108 Right: Superposition of the G_i free MD snapshot and the G_i-coupled cryo-EM structure. The
1109 residues used for the distance measurement in the density plot, $T93^{2.39}$ and $G330^{8.47}$, are shown
1110 as sticks and spheres, respectively. The larger degree of the H8 rotation and the consequent
1111 insertion of the TM7-H8 loop open the gap between H8 and TM6 in the CCL19-bound CCR7
1112 compared to the CCL21-bound CCR7. (B) Structural basis of the distinct H8 orientation between
1113 CCL19-bound CCR7 and CCL21-bound CCR7 in the G_i free MD simulations. The closer positioning
1114 of H8 towards ICL1 and TM2 in CCL19-bound CCR7 is stabilized by the salt-bridge network of
1115 $R88^{12.49}$ to $D94^{2.40}$ and $D336^{8.53}$. The frequency of the salt-bridge formation between $R88^{12.49}$
1116 (ICL1) - $D94^{2.40}$ (TM2) and between $R88^{12.49}$ (ICL1) - $D336^{8.53}$ (H8) during the MD simulations is
1117 shown (middle, the salt-bridge distance threshold of 4 Å). A close-up view of H8, TM1, ICL1, and
1118 TM2 in the MD snapshots of CCL19-bound CCR7 (left) and CCL21-bound CCR7 (right). The
1119 residues of interest are shown as sticks, and salt bridges are shown in dashed lines. (C,D) Effects
1120 of the salt bridge mutations on G_{i1} and β-arrestin2 signaling induced by CCL19 and CCL21. G_{i1}
1121 dissociation and β-arrestin2 recruitment in response to (C) CCL19 or (D) CCL21 at WT, R88A,
1122 D94A, and D336A CCR7. Representative concentration-response curves are shown in the top
1123 panels, while potency ($logEC_{50}$) and efficacy (span; Top-Bottom) are presented as bar graphs in
1124 the bottom panels. Because a clear plateau was not achieved for β-arrestin2 recruitment in
1125 response to CCL21, $logEC_{50}$ and span values could not be reliably estimated and are therefore
1126 not determined. Concentration-response curves represent a single experiment performed in
1127 triplicate and are shown as mean ± SD. Summary data represent three independent
1128 experiments and are shown as mean ± SEM. Statistical analysis was performed using one-way
1129 ANOVA followed by Dunnett's multiple comparisons test versus WT (* $P < 0.05$; ** $P < 0.01$).
1130 Exact P values are shown when $0.05 < P < 0.1$.

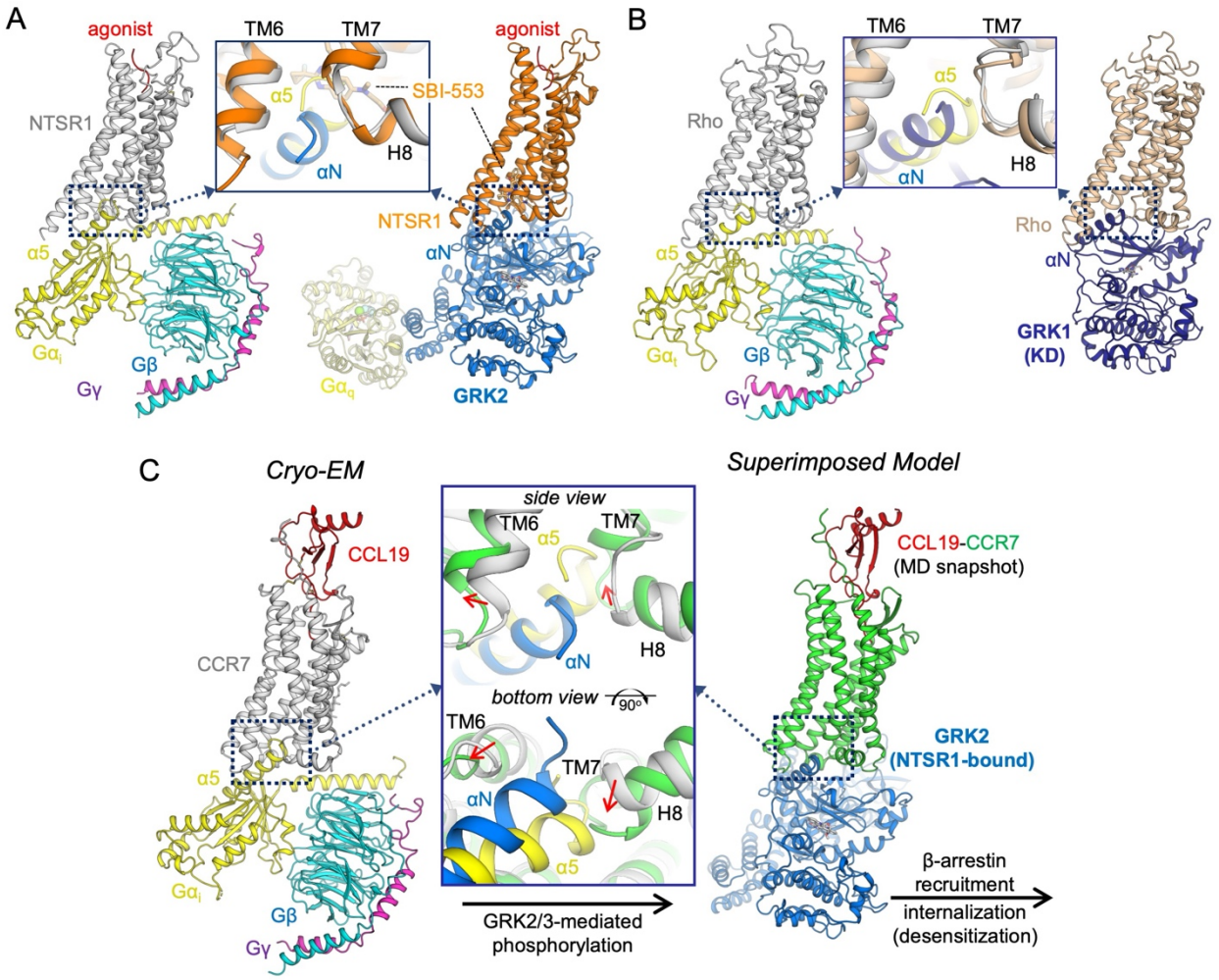

Fig. 6 | Comparison of G protein and GRK binding modes and a structural model for CCR7 biased agonism.

(A) Cryo-EM structures of Neurotensin Receptor 1 (NTSR1) in complex with G_i (PDB: 6OS9, left) and GRK2 (PDB: 8JPB, right). The zoomed-in inset shows a superposition of the two complexes, aligned on the receptor (NTSR1), to directly compare the binding modes of the C-terminal α5 helix of the Gα subunit (yellow) and the N-terminal αN helix of the GRK (blue). (B) Cryo-EM structures of Rhodopsin (Rho) in complex with G_t (PDB: 6OY9, left) and GRK1 (PDB: 7MTA, right). The zoomed-in inset shows a superposition of the Rho-G_t and Rho-GRK1 complexes, aligned on the receptor (Rhodopsin), to compare the effector helices. Both (A) and (B) highlight that while both effectors engage the receptor's cytoplasmic core, the GRK-αN helix exhibits a shallower insertion than the Gα-α5 helix (yellow) and follows a distinct trajectory, exiting through the interface formed by TM6, TM7, and H8. (C) Proposed structural model for the biased activation of GRK2/3 by CCR7. Cryo-EM structure of the CCL19-CCR7-G_i complex (this study, left) and a superimposed model illustrating the proposed mechanism of CCR7-GRK2 engagement (right). The model was generated by superimposing a representative "open" conformation of CCL19-CCR7 (green), derived from MD simulations (Fig. 5A), onto the NTSR1 receptor of the cryo-EM NTSR1-GRK2 complex (PDB 8JPB). The zoomed-in inset compares the G_i-bound state (gray helices, Gα-α5 in yellow) with the modeled 'open' GRK-bound state (green helices, GRK-αN in

1150 blue). This illustrates that the "open" state, stabilized by CCL19-induced H8 dynamics after G
1151 protein dissociation, creates a wide gap between TM6 and H8, which appears sterically
1152 complementary to accommodate the GRK-αN helix. This simple model suggests that CCL19-
1153 induced dynamics selectively favor this "open" ensemble, facilitating efficient GRK2/3
1154 recruitment and robust β-arrestin signaling.